# Mechanical conditions preventing live cell extrusion during primary neurulation in amniotes

Santiago A. Bosch-Roascio[1,2], Julio A. Hernández[2], Flavio R. Zolessi[1,3,*]

1- Sección Biología Celular, Facultad de Ciencias, Universidad de la República, Uruguay.
2- Sección Biofísica y Biología de Sistemas, Facultad de Ciencias, Universidad de la República, Uruguay.
3- Institut Pasteur de Montevideo, Uruguay.

* Corresponding author: fzolessi@fcien.edu.uy

**Keywords:**

neuroepithelium; chick embryo; vertex models; mechanobiology; cell polarity; MARCKS

**Highlights:**

- PMA treatment induces live apical cell extrusion in the chick embryo neural plate
- Our energy-based vertex model mechanically simulates a pseudostratified epithelium
- Higher apical/basal compared to lateral surface tension leads to epithelial stability
- Lower apical/basal surface tension leads to epithelial instability and cell extrusion
- A power law between cell density and surface tension defines the stability threshold

**Abstract**

During primary neurulation in amniote embryos, the neural plate gives rise to the neural tube in a process requiring the coordination of forces at different scales throughout a geometrically complex tissue. The ways in which this process fails inform us of the complex mechanical conditions required for its correct completion. Previous results showed that the functional disruption of MARCKS, a protein which simultaneously interacts with the plasma membrane and actin filaments, resulted in neural tube closure defects with apical cell extrusion. Here, we demonstrate that this is an example of “live cell extrusion”, wherein extruded cells are not undergoing apoptosis. This suggests that extrusion in this case might be due to a mechanical instability in the neural plate. Using an expanded energy-based vertex model of pseudostratified epithelia we then show that extrusion may be elicited by a reduction in the relative surface tension of apical and basal interfaces with respect to cell-cell interfaces. Finally, by considering a continuum description of a simplified epithelium we derive an approximate quantitative threshold for single-layered epithelial stability in the form of a power law relating cell density to the relative value of interfacial surface tensions. Our work serves to explain an example of how alterations in polarization and forces at the single-cell level can produce tissue-scale instabilities which not only greatly alter its morphology but can also ultimately lead to severe developmental defects.

## 1. Introduction

In vertebrates, the central nervous system almost entirely derives from a specialization at the dorsal ectoderm, termed the neural plate, an epithelium that eventually deforms to ingress into the embryo as a whole and forms the neural tube. Particularly in amniotes, this "primary neurulation" process involves the invagination and folding of the neuroepithelium along the cephalo-caudal axis of the embryo to become a tube separated from the epidermal ectoderm that remains at the surface. The series of morphogenetic movements that drive neurulation arise from intrinsic and extrinsic forces exerted over the neuroepithelial cells, which all along the process remain cohesive and highly polarized (Colas and Schoenwolf, 2001; de Goederen et al., 2022). The intrinsic forces deforming the neural plate are generated at different levels, including actions mediated by the cytoskeleton. In addition, forces extended along several cells in the neural plate, such as those generated by convergent-extension movements (Schoenwolf and Smith, 1990), or coming from the surrounding non-neural ectoderm (Alvarez and Schoenwolf, 1992; Moury and Schoenwolf, 1995), could contribute to bending. In this regard, the early work by Lee and Nagele has indicated that neural plate-intrinsic forces would be sufficient for the formation of the neural tube in chick embryo explants (Lee and Nagele, 1988).

All these forces are applied to cells that, in addition, greatly increase their proliferation rate from the neural plate stage on, becoming a quickly growing population (Copp and Greene, 2010). Cells remain attached to both apical and basal surfaces, but they increase their height and reduce their width, generating a tall pseudostratified epithelium. In this organization, cells display interkinetic nuclear migration, by which cell divisions occur at the apical border of the neuroepithelium, while S-phase tends to occur in nuclei closer to the basal side (Norden, 2017; Sauer, 1936). The combination of all these factors results in neuroepithelial cells with extremely complex shapes (Gómez et al., 2021; Iber and Vetter, 2022).

How is it possible that this epithelial cell population tolerates the enormous forces that drive neurulation while proliferating at a high rate, without disruption? Different lines of evidence indicate that the key might be in the strict maintenance of apico-basal cell polarity. Among other factors, this is achieved through a tight binding of each cell to the basal lamina on the basal side, and to their neighboring cells at the sub-apical border through integrin- and cadherin-based cell adhesions, respectively (Saade and Martí, 2025). These adhesion complexes tightly, but dynamically, bind to the cytoskeleton, establishing a mechanically

96 continuous meshwork that spans across cells, and that can be modulated in response to
97 different external and internal cues (Campàs et al., 2024; Sluysmans et al., 2017; Zhang and
98 Wei, 2025). It has been generally accepted that microtubules extend during neurulation,
99 elongating cells along the apico-basal axis, while the actin cytoskeleton acts in different ways,
100 allowing cells to take a wedge-like shape (Cearns et al., 2016; Schoenwolf and Powers, 1987).
101 The maximal accumulation of actin filaments is observed close to the apical cell border, in
102 association with the cadherin-based *zonula adherens*, and acto-myosin contraction at this
103 level has been indicated as an important motor in apical surface reduction (Ampartzidis et al.,
104 2023; Escuin et al., 2015; Martin and Goldstein, 2014; Sawyer et al., 2011). This apical
105 constriction would be more relevant in highly-bent areas of the neural plate, when they exist,
106 such as the ventromedial and the dorso-lateral hinges. Here, other cell processes, like basal
107 positioning of nuclei and localized programmed cell death were also shown to contribute to
108 epithelial bending, highlighting the importance of regulating cell crowding during neurulation
109 (Roellig et al., 2022; Smith and Schoenwolf, 1988).
110 It is not surprising, then, that several polarized actin-modulating proteins have been
111 demonstrated to be necessary for primary neurulation. Among these are the MARCKS family
112 members. MARCKS (Myristoylated Alanine Rich C-Kinase Substrate) and MARCKS-Like 1 are
113 ubiquitous proteins present only in vertebrates, which simultaneously interact with the
114 plasma membrane and actin filaments (Arbuzova et al., 2002; El Amri et al., 2018).
115 Phosphorylation by PKC (or interaction with calcium-calmodulin) causes MARCKS to detach
116 from the membrane and to lose one of the two actin-binding sites (McLaughlin and Aderem,
117 1995). Hence, MARCKS acts as a molecular switch connecting extracellular signals to the cell
118 cortex. Disruption of MARCKS family protein expression causes severe neurulation defects in
119 both mice and zebrafish embryos (Chen et al., 1996; Prieto and Zolessi, 2017; Stumpo et al.,
120 1995). Further, we found that MARCKS is accumulated at the apical membrane in neural plate
121 cells of the chick embryo only during neural tube closure, and that its knockdown causes a
122 failure of neural tube closure (Aparicio et al., 2018; Zolessi and Arruti, 2001). Interestingly,
123 the local cellular phenotype observed in these embryos was very similar to the effect obtained
124 after treatment with a strong agonist of PKC, the phorbol ester PMA: loss of apico-basal cell
125 polarity accompanied by apical cell extrusion. This effect of PMA was effectively rescued by
126 the expression of a non-phosphorylatable form of MARCKS, where all serines at the ED were
127 substituted by asparagines (Aparicio et al., 2018).

128 Apical cell extrusion, that is, the expulsion of a cell through the apical side of the epithelium,
129 has been generally reported as an active mechanism for maintaining epithelial density and
130 integrity, and involves biochemical and mechanical signaling such as the secretion of
131 sphingosine-1-phosphate (S1P) by extruding cells, which activates Rho and actomyosin in
132 neighboring cells (Eisenhoffer and Rosenblatt, 2013; Nanavati et al., 2020). One function of
133 this process is the elimination of dying cells from the epithelium ("apoptotic cell extrusion"),
134 and implies medium-scale epithelial topological irregularities, pulsatile contractions and loss
135 of tissue tension (Atieh et al., 2021; Saw et al., 2017), together with the local activation of
136 lamellipodial protrusions and the assembly of a basally-localized contractile actomyosin ring,
137 in a cadherin-dependent manner (Duszyc et al., 2021; Lubkov and Bar-Sagi, 2014; Rosenblatt
138 et al., 2001). Conversely, "live apical cell extrusion" appears as a counterbalancing mechanism
139 to avoid cell overcrowding in a proliferating cell population, and occurs regularly in many
140 physiological processes of epithelia, like in cell shedding in intestinal microvilli and in the
141 control of carcinogenic transformation (Madara, 1990; Tanimura and Fujita, 2020). It requires
142 stretch-activated ion channels (Piezo), S1P and the Rho-myosin pathway, and also produces
143 regular topological changes in the organization of the epithelium, based on the collective
144 action of surrounding cells (Eisenhoffer et al., 2012). During this type of extrusion, the cell
145 being expelled remains alive and plays an active part in the process, eventually dying by
146 anoikis after the extrusion has been completed (Marinari et al., 2012; Slattum and Rosenblatt,
147 2014).
148 Taking all this information, we wondered if apical cell extrusion of neuroepithelial cells upon
149 MARCKS knockdown or PKC activation could be a live cell extrusion mechanism related to an
150 imbalance in the mechanical forces in the cell population. This could be caused either by the
151 alteration of the actin cytoskeleton or by the downregulation of apico-basal cell polarity. By
152 pharmacologically inhibiting caspase activity on PMA-treated chick neurulas, we demonstrate
153 here that the observed massive apical cell extrusion is mediated by a live mechanism.
154 Secondly, we aimed at explaining the experimental observations by generating a theoretical
155 model and performing computational simulations. We present an expanded 2D vertex model
156 of a pseudostratified epithelium, to show that alterations in the balance of forces imposed to
157 cells on the apical or basal plasma membrane domains compared to lateral domains, was
158 enough to robustly obtain situations that could only be solved by massive cell extrusion.
159

160 **2. Methods**

161 **2.1. Embryo culture**

162 Wildtype chicken eggs were provided by a local producer (PRODHIN) and incubated at 37° C
163 for at least 28 h, corresponding to stage HH 8 (Hamburger and Hamilton, 1951). Chick
164 embryos were cultivated *ex ovo* with ventral side up over a semi-solid agar/albumen substrate
165 in 35 mm Petri dishes using the EC culture technique (Chapman et al., 2001). Cultured
166 embryos corresponding to stages lower than HH8-/8 were incubated until they reached the
167 desired stage. A total of 72 embryos were processed, spread across five experiments.

168

169 **2.2. Pharmacological treatments**

170 Cultured embryos were divided into four groups according to treatment: those receiving
171 treatment with PMA, QVD-OPh, neither (control) or both (double, PMA+QVD). Stock solutions
172 were prepared for PMA (Sigma-Aldrich P-8139) at 5 mM and QVD-OPh (MedChem Express
173 #HY-12305) at 20 mM, both diluted in 100% DMSO.

174 All embryos were pre-incubated for 30 min. at 37° C with a 20 µl drop containing either 0,83
175 % DMSO in 1x PBS (control and PMA) or 167 µM QVD-OPh (1:120 dilution; QVD-OPh and
176 double), applied ventrally. Afterwards, the excess liquid was removed and embryos were
177 moved to a new culture dish containing 0.93% DMSO (control), 5 µM PMA (1:1000 dilution)
178 and 0.83% DMSO (PMA), 167 µM QVD-OPh and 0.1% DMSO (QVD-OPh) or PMA and QVD-OPh
179 (double) embedded in the substrate. Additionally, a new 20 µl droplet containing either
180 DMSO or QVD-OPh was applied as before. Embryos were then incubated for 3 h at 37° C.

181

182 **2.3. Cryo-sections**

183 After incubation, embryos were collected and fixed in 4% paraformaldehyde (PFA, in 1x PBS)
184 at 4° C overnight. Excess tissue was then cut and excess PFA was removed by washing 3x with
185 1x PBS for 1 h. Embryos were cryoprotected by being incubated first in a 5% sucrose/PBS for
186 3 h and then in a 20 % sucrose/PBS solution at 4° C overnight, and were then embedded in a
187 medium containing 7.5 % gelatin and 15 % sucrose dissolved in PBS, in a 35 mm Petri dish.
188 Gelatin was left to set at room temperature and then stored at 4° C for up to a few days.
189 Blocks were cut from these media and frozen using liquid nitrogen. 10 µm transversal slices

190 were cut from these blocks using a cryostat (Reichert-Jung Cryocut E) at -21° C and placed
191 onto gelatinized microscope slides (0.5 % gelatin, 0.05% chrome alum in water).
192
193 **2.4. Immunofluorescence**
194 Indirect immunofluorescence on the slices was performed following (Stern and Holland,
195 1993). All antibodies were diluted in a 1 % BSA/PBS solution. Primary antibodies used were
196 rabbit anti-MARCKS (1:1000, Toledo et al., 2013), rabbit anti-cleaved Caspase 3 (1:200, Cell
197 Signaling Technologies #9661), rabbit anti-ɣ tubulin (1:100, Sigma-Aldrich #T5192) and mouse
198 anti-ZO-1 (1:50, Invitrogen #33-9100). Secondary antibodies used were anti-rabbit Alexa 488
199 (1:500, Invitrogen #A21206) and anti-mouse Alexa 488 (Invitrogen #A11001). Phalloidin-TRITC
200 (1:8000-10000, Sigma) was included during the incubation with secondary antibodies.
201 Hoechst 33342 DNA staining was performed during the final PBS washes.
202
203 **2.5. Image Acquisition and processing**
204 Slices were mounted for imaging using 70 % glycerol in Tris buffer (20 mM, pH 8), covered
205 with a coverslip and sealed using nail polish. Imaging was performed on a confocal Zeiss LSM
206 800 microscope using a 20x (dry, NA = 0.8) or 25x (glycerol immersion, NA = 0.8) objective
207 lens. Images consisted of stacks of optical sections every 1 µm, in slices corresponding
208 approximately to the fourth somite. Image processing and analysis was done using FIJI
209 (Schindelin et al., 2012).
210
211 **2.6. Cell extrusion and cell death quantification**
212 In order to determine the number of embryos exhibiting cell extrusion and indications of cell
213 death (pyknotic nuclei and cleavage of caspase 3), mounted slices were examined under a
214 Nikon Microphot FXA epifluorescence microscope, using 20x (dry, NA = 0.75) and 40x (dry,
215 NA = 0.95) objective lenses. Extruded cells were identified as lying apical to the actin
216 accumulation line corresponding to the apical side of the neuroepithelium in normal
217 conditions, occasionally checking nuclear staining for confirmation. In order to determine that
218 an embryo had not experienced any cell extrusion, four different nearby slices were checked.
219 Counting of pyknotic nuclei and cells showing cleaved caspase 3 (i.e.: those labelled with the

220 anti-cleaved caspase 3 antibody) was done in four nearby (non-damaged) slices of each
221 embryo and adding the resulting numbers.
222
223 **2.7. Protein distribution quantification**
224 Starting with stacks of optical sections, distribution of fluorescent signals was determined
225 from average intensity projections of three slices. Our region of interest was the mostly flat
226 section of the neural plate adjacent to the medial hinge. Images were then rotated so as to
227 make the apical side of our region of interest face left, and from there, the fluorescence
228 profile was obtained along an approximately 20 µm wide transect (71 px, corresponding to
229 20.09 µm). Background signal intensity was obtained as the mean intensity of a 40 px square
230 outside the tissue and subtracted from all values.
231 Phalloidin intensity profiles in control embryos typically showed two peaks corresponding to
232 the basal and apical side of the tissue respectively, which we used to define these regions in
233 the apico-basal axis. The apical region was defined as the interval within 9 px (2.5 µm) of the
234 appropriate phalloidin signal maximum, which was observed to correspond approximately to
235 a 50 % decrease in signal intensity in control embryos. The sub-apical region was defined as
236 the interval between the basal phalloidin maximum and the apical region. In cases with
237 cellular extrusion more apical peaks were observed, but a peak corresponding to the apical
238 side of non-extruded cells was usually identifiable. Analysis of the tissue morphology was used
239 to clear any doubts regarding multiple possible basal or apical peaks.
240 The ratio of apical to sub-apical signal for MARCKS and ZO-1 immunostaining was then
241 calculated as the largest value found in the apical region divided by the average value in the
242 sub-apical region.
243
244 **2.8. Statistical analysis**
245 Statistical analyses were performed for the values for the ratio of the maximum
246 immunofluorescent signal intensity in the apical regions relative to the average signal
247 intensity of the sub-apical region for both MARCKS and ZO-1 for each experimental condition,
248 using GraphPad Prism (version 8.0.2 for Windows; GraphPad Software, Boston,
249 Massachusetts USA, www.graphpad.com). All distributions passed the Shapiro-Wilk,

Anderson-Darling and D'Agostino & Pearson lognormality tests ($\alpha = 0.05$), with the exception of the MARCKS distribution in control embryos, in which N was too small for the Anderson-Darling and D'Agostino & Pearson tests. Differences of means between pairs of experimental conditions were determined using Welch's t-test for the natural logarithm of the presented values.

**2.9. Theoretical description**

We based our model on the augmented vertex model previously described by Kim et al. (2021, 2024), in which cell-cell interfaces are represented by vertices joined by straight edges, and nuclei are represented as solid-like objects constrained by the cell membrane. While this kind of model has usually been used to represent the apical surface of epithelia, our work represents the epithelium as a lateral cross-section, similar to those presented in the experimental results. Our 2D model is based on an energy functional (Eq. 1) depending on all cell areas, the length of all cell-cell (or cell-exterior milieu) interfaces and the total "overlapping" radial distance of a cell's nucleus with respect to its membrane, integrated along the cell's contour.

$$E = \sum_{i,j} T_{ij} L_{ij} + \sum_{i} K \left( \frac{A_i}{A_0} - log\left(\frac{A_i}{A_0}\right)\right) + \frac{1}{2} K_n \oint_{\partial C_i} (R_i(s) - r_i(s))^2 H(R_i(s) - r_i(s))\, ds \qquad (1)$$

where $L_{ij}$ and $T_{ij}$are the length and the surface tension of the interface between cells $i$ and $j$ respectively, $K$ is the cell compressibility modulus which measures how much pressure the cell exerts while being compressed, $A_i$ is the area of cell $i$, $A_0 = K/P_0$ is a characteristic area based on $P_0$ the external medium's pressure, $K_n$ is the nuclear elastic modulus which determines the repulsion force generated when the nucleus overlaps the cell boundary, $r_i(s)$ is the distance measured from the center of the nucleus of cell $i$ to a point in the cell boundary $\partial C_i$ (parametrized by arc-length $s$), $R_i(s)$ is the distance between the nuclear center and its border in the same direction, and $H(x)$ is the Heaviside function, which ensures only points in which the nucleus overlaps its cell's membrane are included in the line integral (taken over cell's $i$ membrane $\partial C_i$). The first sum is over all cell-cell (and cell-exterior) interfaces $ij$, the second one over all cells $i$. Note that in the case of a circular nucleus, $R_i(s)$is simply the nucleus' radius (see a graphical description in Figure 1).

280 **2.10. Simulations**

281 All simulations were based on a non-dimensionalized version of $E$ (Equation 1; Appendix A.1)
282 defining certain characteristic scales: $P_0$ (pressure of the external medium), $T_0$ (surface
283 tension of cell-cell interfaces), $L_0 = \sqrt{A_0} = \sqrt{K/P_0}$ (characteristic length-scale) and $\tau_R$
284 (characteristic timescale for vertex relaxation). When not explicitly stated, we followed Kim
285 et al. (2024) in their estimation for all corresponding parameters. Assuming a viscous medium
286 where frictional forces dominate, the positions of all vertices follow first-order differential
287 equations in which velocities are proportional to the sum of all non-viscous external forces
288 (Odell et al., 1981). These forces may be obtained as the negative gradient of $E$ with respect
289 to their respective positions. The same can be applied to nuclei, which are defined as solids
290 by their centers of mass and rotation angles, with this last variable being ignored by
291 considering only circular nuclei in all simulations.

292 Dynamic simulations were carried out using custom scripts written for GNU Octave (Eaton et
293 al., 2020) by numerically integrating these first-order differential equations using the Euler
294 method with a time step $\Delta t = 0.005\,\tau_R$. Unless stated otherwise, all simulations were
295 initialized with periodic boundary conditions of length $\lambda = 10$ and with $N = 20$ rectangular
296 cells of area 1, a limit of our computational implementation. Edge length was maintained by
297 adding or joining vertices between 1/16 and 1/8 of the average cell width, defined as $b =$
298 $\lambda/N$. In the cases in which this resulted in the formation of a 4-fold vertex, a T1 transition
299 (neighbour exchange; necessary for extrusion in our model) was evaluated and computed
300 using the method described by (Duclut et al., 2021). The surface tension of all apical and basal
301 interfaces was defined as $T_a$, relative to $T_0$. Whether the system had reached an equilibrium
302 state was determined by qualitatively checking whether the energy had stabilized to a
303 minimum over time.

304 In addition to these dynamical simulations, we analyzed the dimensionless energy minima for
305 a simplified tissue made up of wedge-shaped cells without nuclei under different values of
306 parameters $T_a/T_0$ and $b$ (inversely related to the tissue's cell density).

307

308

309

310 **3. Results**

311 **3.1. Experimental assessment of the mode of apical cell extrusion in PMA-treated embryos**

312 With the aim of elucidating if the PMA-induced apical cell extrusion in the neural plate was
313 live or apoptotic extrusion, we set up the conditions for treating neurulating chick embryos
314 simultaneously with PMA and the pan-caspase inhibitor QVD-OPh. Since both drugs must be
315 administered solubilized in DMSO, and given the relatively low dilution rate needed for QVD-
316 OPh, we used the lowest possible amount of DMSO which did not cause obvious effects on
317 embryo or cell survival: 0.93%. In these conditions, control embryos developed normally, not
318 showing delays in general development or neurulation (Fig. 2A). Widespread apical cell
319 extrusion was observed throughout the neural plate in all embryos treated with PMA (n = 20)
320 and those treated with both PMA and QVD-OPh (n = 20), while no cell extrusion was observed
321 in control embryos (n = 15) or those under QVD-OPh treatment alone (n = 17) (Fig. 2B).

322 As expected, PKC activation with PMA caused in all cases a redistribution of MARCKS from the
323 plasma membrane to the cytoplasm, in addition to a loss of its apical accumulation (Fig. 3A).
324 QVD-OPh-only treated embryos, on the contrary, showed a MARCKS distribution that
325 resembled control embryos. To further check the effect of these treatments on apico-basal
326 polarity, we decided to analyze the distribution of the sub-apical cell adhesion–associated
327 protein ZO-1. As previously reported (Aparicio et al., 2018), PMA treatment provoked a clear
328 loss of apical accumulation of this apical marker, and this was not affected by co-incubation
329 with QVD-OPh (Fig. 3B). In order to compare apical protein accumulation across the different
330 treatments, we measured the ratio of apical signal with respect to the average sub-apical
331 signal intensity for both proteins, MARCKS and ZO-1 (see section 2.7). QVD-OPh-only-treated
332 embryos showed a similar distribution to control embryos, while those treated with PMA
333 exhibited a significant decrease in apical protein accumulation (Fig. 3C). Similarly, double
334 treated embryos showed a significant difference with respect to embryos treated only with
335 QVD-OPh. These results further indicated that treatment with the anti-apoptotic drug did not
336 affect cell extrusion or cell polarity by itself.

337 DNA staining indicated the presence of few scattered apparently dying cells in all embryonic
338 tissues, at all treatment conditions. But, as previously described (Aparicio et al., 2018), PMA
339 treatment greatly increased the number of pyknotic nuclei mostly on cells extruded from the
340 neural plate (see Fig. 3B, for example). This was confirmed by immunolabeling of activated

341 Caspase 3 (Fig. 4A). Most of these dying cells were observed beyond the apical border of the
342 mass of extruded cells, indicating they were detaching from the epithelium. The double
343 treatment of embryos with PMA and QVD-OPh, on the other hand, showed a sharp reduction
344 in cell death as assessed by quantifying both parameters, demonstrating that the observed
345 apical extrusion happens independently of cell death in these embryos, and can be defined
346 as live cell extrusion (Fig. 4B).

347

348 **3.2. Computational model of a pseudostratified epithelium and conditions leading to cell**
349 **extrusion in the simulation**

350 Since our experimental results support the idea that PMA treatment causes live cell extrusion
351 during development, we focused on determining the conditions under which an epithelium
352 like the neural plate could become mechanically unstable, leading to the elimination of live
353 cells from the tissue. Our first goal was to produce a model which could reproduce the
354 morphology of pseudostratified epithelia, that is, a single layer of columnar cells in which the
355 nucleus occupies a large proportion of the cell volume, resulting in curved cell-cell interfaces
356 shaped so as to accommodate all nuclei at different heights along the apico-basal axis. We
357 are not considering in the model the continuous cell shape changes that would be caused by
358 interkinetic nuclear migration in a living neuroepithelium because the experimental time-
359 scale of the PMA-induced cell extrusion (less than 3 h) is much shorter than the average
360 extension of the cell cycle in this cell population (8-12 h; Schoenwolf, 2018).

361 In order to achieve this, we developed a modification of the augmented vertex model
362 originally described by Kim and collaborators to represent the dynamics of epithelia from an
363 apical point of view (Kim et al., 2024, 2021). In our version of the model, we chose to represent
364 a lateral view of an epithelial tissue under periodic boundary conditions (Fig. 5A). The model
365 consists of a set of cells and solid-like nuclei for which an energy functional $E$ is defined, which
366 depends on the different cell areas, boundary lengths and position of the nuclei within the
367 cell (see section 2.9 and Equation 1). Although we followed the force-based model of Kim et
368 al. (2021, 2024) in defining this energy, the forces arising from our description are not
369 necessarily identical to theirs, particularly in the case of the nuclear repulsion forces (for
370 example, our calculations are based on vertices, not edges; see Appendix A.3). It can be
371 proven that in the absence of nuclear repulsion forces, the angle between adjacent edges at

372 equilibrium depends only on the interface they belong to (Appendix A.2). As a corollary, all
373 interfaces not overlapping with a nucleus should approximate circular arcs at equilibrium. This
374 indicates that an equilibrium state resembling a pseudostratified morphology could only be
375 observed in cells with nuclei larger than the average cell width $b$, defined in this model as the
376 dimensionless length of the tissue in the *x*-axis divided by the total number of cells. Supporting
377 this, our initial dynamical simulations showed that cell layers containing no nuclei reached an
378 equilibrium state consisting of identical columnar cells with straight cell-cell and convex cell-
379 medium interfaces (Supplementary Fig. 1). This happened in less than twice the characteristic
380 timescale for vertex relaxation $\tau_R$.

381 Based on the previous considerations, we followed by performing initial exploratory
382 simulations including wide nuclei distributed alternatingly in the model, so that a cell with an
383 "apical nucleus" (tangent to the initial apical boundary) has neighbors with "basal nuclei" and
384 vice versa (Fig. 5B). Ratios of the apical/basal surface tension ($T_a$) with respect to lateral
385 surface tension ($T_0$) of 1.5 or lower led to variable extensions of cell extrusion, with cells losing
386 either their apical or basal interfaces, depending on their initial nuclear position, and
387 stabilizing into a more rounded shape (Fig. 5B). Larger values of $T_a/T_0$, on the other hand,
388 allowed for the tissue to stabilize into a single layer of columnar cells with curved cell-cell
389 interfaces determined by the position of nuclei, corresponding to the pseudostratified
390 morphology we sought (Fig. 5B). At values just above this threshold, cells formed a single layer
391 but stabilized into a wedge-like shape with straight cell-cell interfaces, as would be expected
392 in the absence of nuclei or with nuclei located in a region of the cell wider than itself (see Fig.
393 5B for $T_a/T_0 = 2$). Parameters $b = 0.5, T_a/T_0 = 5$ prevented extrusion also in simulations
394 initialized under different nuclear distributions (Fig. 5C-E).

395

396 **3.3. Analysis of energetic minima in a simplified model**

397 While the dynamical described simulations suggest a qualitative relation between relative
398 surface tensions ($T_a/T_0$) and extrusion, we could not clearly express it in quantitative terms.
399 Furthermore, we are limited by our computational implementation in the parameter ranges
400 we can study, as well as by our lack of experimental measurements of these parameters in
401 this particular tissue. For example, even though we know the neural plate is a highly dense

402 tissue and suspect that this high density may be related to cell extrusion, we cannot perform
403 dynamical simulations to directly test this for our system.

404 To avoid these limitations, we looked for general stability conditions by constructing a
405 simplified version of our model for which we could better analyze equilibrium states and
406 stability. Based on the results obtained from simulations with alternating nuclei, we
407 considered a single-layered tissue formed by alternating wedge-shaped cells without nuclei
408 (Fig. 6A; see Appendix A.4). We assume these cells to have continuous straight cell-cell
409 boundaries (i.e.: no vertices), and their apical/basal interfaces to be circular arcs. Equations
410 can be derived for such a tissue in terms of two geometrical variables: cell height ($h$) and basal
411 width ($b_b$), under parameters $T_a/T_0$ (apical/basal surface tension relative to lateral surface
412 tension), $b$ (average cell width, the inverse of cell density) and $L_0$ (characteristic length,
413 related to the cell compressibility module $K$). Setting $L_0 = 10\,T_0/P_0$ initially as in our
414 dynamical simulations, we numerically computed the energy landscape for different cell
415 shapes. Assuming the final area will be less than 1, we considered $0 \leq h \leq 1/b$ and $0 \leq b_b \leq$
416 $2b$, between the limits where apical and basal extrusion occur. From these, we found the
417 values of $h$ and $b_b$ which minimized the energy of the system for different values of
418 parameters $b$ and $T_a/T_0$, and searched for ways in which these might be related to extrusion
419 or to single-cell layer stability.

420 We observe that this system is symmetrical in that a tissue with basal width $b_b$ is equivalent
421 to one with basal width $2b - b_b$, and that an energy minimum with $b_b = 0$ would lead either
422 to extrusion or to a persistent 4-fold vertex, usually considered to be mechanically unstable.
423 In general, low values of $b$ lead to energy minima with $b_b = 0$, and high values of $b$ lead to
424 $b_b = b$, with an intermediary transition range (Fig. 6B). For high values of $T_a/T_0$, this creates
425 an apparently clear division of the $b$ range into three connected regions, but this is not the
426 case for lower values ($T_a < 0.8\,T_0$, approximately), for which deviations may be observed. For
427 example, low values of $b$ may have a non-null equilibrium basal width $b_b$.

428 The cases in which $b_b = b$ correspond to a symmetrical equilibrium state which may be found
429 in simulations when cells do not interact with the nuclei (Supplementary Fig. 1). This state
430 always exists as a possible equilibrium solution, as equations for it can be found for all values
431 of $b$ as long as $T_a/T_0 > 0.5$ (Appendix A.5). We may define $b_0(T_a/T_0)$ as the maximum value

of $b$ for which the energy minimum occurs at $b_b = 0$ (or $2b$, equivalently) and $b_1(T_a/T_0)$ as the minimum value of $b$ for which the energy minimum occurs at $b_b = b$.

Plotting both $b_0$ and $b_1$ against $T_a/T_0$ divides the parameter space into three regions according to the different long-time behaviours of the system (Fig. 6C). The upper region corresponds to $b_b = b$ (stable monolayer composed of columnar cells of constant width), whiled the lower region corresponds to $b_b = 0$ (leading to extrusion). The distance between them tends to 0 for large $T_a/T_0$ values. We observe that $b_1(T_a/T_0)$ follows a power-law equation (Fig. 6D), and that the same can be said of $b_0(T_a/T_0)$ for sufficiently large values of $T_a/T_0$, obtaining equations

$$b_0 = k_0 \left(\frac{T_a}{T_0}\right)^{-\alpha_0} \quad and \quad b_1 = k_1 \left(\frac{T_a}{T_0}\right)^{-\alpha_1} \tag{2}$$

with $k_0 = exp(-0.4237) \approx 0.65$, $\alpha_0 = 0.5612$ (linear fit of log-log data with $R^2 > 0.998$ for $T_a/T_0 > 1.6842$) and $k_1 = exp(-0.3729) \approx 0.69$, $\alpha_1 = 0.5761$ (linear fit of log-log data with $R^2 > 0.999$). It should be noted that these values depend on the remaining parameter, the cell compressibility modulus $K$, with $k_0$,$k_1$ increasing and $\alpha_0$, $\alpha_1$ decreasing as $K$ increases, seemingly reaching an asymptote (Supplementary Fig. 2). We could not find similar simple equations for other geometric parameters which might characterize the stability of the system, such as the cell height or aspect-ratio ($b/h$) at equilibrium.

### 3.4. Dynamic simulations of pseudostratified epithelia in conditions of near instability

Because of our simplification, this classification does not take into account the nuclear repulsion forces. Nevertheless, we may reasonably assume that for a system with nuclei to have a stable one-layered equilibrium state, it should also be stable in the absence of nuclei. Namely, in a highly dense tissue, where $b$ is low and $h$ is high, nuclei may be wider than $b$ but much shorter than $h$, in which case they would only interact with a small number of vertices. If this approximation is correct, then the curve $b_0$ should allow us to predict the threshold value of $T_a/T_0$ needed to stabilize a tissue for a given $b$ even in the presence of nuclei. Our data show that $b_0$ reaches a global maximum of $b = 0.6040$ between $T_a/T_0 = 0.8$ and $0.8167$, meaning: (1) that extrusion should not happen in any system with $b > 0.6040$ and (2) that every value $b < 0.6040$ has two possible threshold values for extrusion. We tested both

situations by performing dynamical simulations using $b = 0.5$ and $b = 10/16 = 0.625$ (Fig. 7A).

Our data predict that $b_0 = 0.5$ when $T_a/T_0 = 1.527$ (Fig. 7A), meaning that systems with $b = 0.5$ should be unstable for $T_a/T_0 \leq 1.527$ and stable for larger values, which agrees with our results for alternating nuclei (Fig. 7B,C; Supplementary Videos 1-2). Simulations using different initial nuclear distributions produced mixed results, with extrusion being prevented under a "staircase" distribution but not under random distributions (Fig. 7B) which had shown to be stable far away from this theoretical threshold, at $T_a/T_0 = 5$ (see Figure 5C-E). As mentioned above, there exists another possible threshold value for $b = 0.5$, meaning that extrusion should be prevented in a system with $T_a/T_0 = 0.55$. Nevertheless, extrusion was observed in this case along with simulation artefacts, indicating a limitation of our computational implementation (Fig. 7D). In agreement with our predictions, on the other hand, no extrusion was observed in the case where $b = 0.625$ when starting with an alternating distribution of nuclei, even for a low $T_a/T_0$ value (Fig. 7E,F). Taken together, these results partially validate our approximation but point to a dependence between the initial distribution of nuclei and the actual stability threshold.

484 **4. Discussion**

485 It was previously shown that MARCKS knockdown, or its phosphorylation upon PMA
486 treatment, induced a loss of apico-basal polarity and extensive apical cell extrusion in the
487 neural plate of chick embryos. This happened without an evident increase in cell death, except
488 for cells that appeared completely detached from the epithelium, suggesting a live cell
489 extrusion mechanism (Aparicio et al., 2018). In the present work, we have confirmed this to
490 be the case: cell extrusion covering the full width of the neural plate occurred in all embryos
491 under PMA treatment even when apoptosis was effectively inhibited with the anti-apoptotic
492 drug QVD-OPh. Despite similar amounts of extruded cells, the treatment produced a near-
493 total loss of signs of cell death. This allowed us to conclude that the observed apical cell
494 extrusion occurred independently of apoptosis, indicating this to be an example of live cell
495 extrusion that could be explained by mechanical alterations in the neuroepithelium
496 (Eisenhoffer et al., 2012; Eisenhoffer and Rosenblatt, 2013).

497 Having cleared this point experimentally, we decided to proceed with a theoretical model of
498 the neuroepithelium which could reproduce a pseudostratified morphology and show cell
499 extrusion purely as a product of an imbalance of mechanical forces along the apico-basal cell
500 axis. Previously published models, along with experimental studies, have pointed to losses in
501 apical surface tension, tissue irregularities (i.e.: anisotropy and topological defects) and high
502 in-plane cell densities as important conditions determining the occurrence of cell extrusion
503 (Drozdowski and Schwarz, 2024; Marinari et al., 2012; Okuda et al., 2010; Saw et al., 2017).
504 Excluding apical tension, the mechanical meaning of such predictors becomes difficult to
505 discern in pseudostratified epithelia, where cell density is much higher than in previously
506 considered situations and where cells develop complex three-dimensional shapes and
507 arrangements in order to accommodate high nuclear densities (Gómez et al., 2021).
508 Furthermore, these geometrical characteristics have been largely simplified or ignored by
509 prior models of pseudostratified epithelia (Hecht et al., 2022; Ishii et al., 2021).

510 Although simulated extrusion may not perfectly reflect the *in vivo* mechanisms, we may use
511 the model to find conditions under which a pseudostratified morphology might become
512 unstable in a mechanical sense, leading to a live cell extrusion-like behavior. We found that a
513 low ratio of apical/basal to lateral interfacial surface tension ($T_a/T_0$) led to widespread
514 extrusion, while higher values prevented it. In particular, when wide nuclei (i.e.: wider than

515 the average cell width) were present and $T_a/T_0$ was sufficiently large, the tissue reached an
516 equilibrium state which was reminiscent of a pseudostratified epithelium: a single layer of
517 cells with curved boundaries shaped so as to accommodate all nuclei at different heights
518 along the apico-basal axis.

519 With these considerations in mind, the results obtained from our model would suggest that,
520 under normal conditions, the surface tension in apical and basal interfaces must be larger
521 than that in lateral cell-cell interfaces so as to mechanically stabilize the pseudostratified
522 morphology. To quantitatively assess this, we approximated the stability of cells in a dense
523 tissue where the nucleus mechanically interacts with a small fraction of the cell's surface by
524 analyzing a simple tissue composed of identical wedge-shaped cells without nuclei. Under this
525 simplification, we found that the minimum average cell width $b_0$ required for a tissue with
526 relative apical/basal surface tension $T_a/T_0$ to be stable approximately follows a power law,
527 with parameters depending on the cell compressibility modulus $K$. This approximation, while
528 correct for large values of $T_a/T_0$ or $b$ and certain regular nuclear distributions, was not enough
529 to predict cell extrusion in general, particularly when nuclei had random initial positions which
530 had been shown to be stable under higher $T_a/T_0$ values. These results serve to point out the
531 limitations of our approximation and show that the exact conditions for extrusion may
532 depend on the actual nuclear distribution adopted by the tissue. Unlike alternating nuclei,
533 some configurations require nuclear rearrangements to reach stability, particularly those with
534 initially overlapping nuclei such as the random distributions tested here. In our model these
535 rearrangements would alter the force balance on the cell boundary in complex ways, which
536 may explain these differences in stability thresholds. The importance of nuclear positioning,
537 as well as the forces it exerts on the cell cortex through interactions with the cytoskeleton,
538 have been experimentally demonstrated in different epithelial morphogenetic processes
539 (Ambrosini et al., 2019; Ferme et al., 2025; Roby and Rauzi, 2025).

540 Although the relative simplicity of this theoretical model does not reflect most of the complex
541 features of a real epithelium, the concomitant inclusion of a surface tension and a non-
542 deformable nucleus can be used to simulate morphogenetic processes in which both factors
543 are important (Kim et al., 2024). Deformability is nevertheless an intrinsic property of living
544 cell nuclei, although with some limitations (Kalukula et al., 2022). Interestingly, in the
545 extension of the Drosophila embryo germband, the simultaneous genetic alteration of

546 nuclear deformability and the pharmacological destabilization of microtubules, affecting
547 nuclear positioning in the apico-basal cell axis, causes both morphogenetic defects and cell
548 extrusion (de Leeuw et al., 2024).

549 Based on the previous analysis, we can give an interpretation of our experimental results
550 simply by assuming that PMA treatment alters the relative surface tension of the apical
551 and/or basal interface (e.g.: by diminishing apico-basal polarization in each cell) without
552 altering cell compressibility. The change required to destabilize the single-layered
553 morphology of the tissue would imply reducing $T_a/T_0$ so that the new minimum stable cell
554 width ${b_0}^{PMA}$ became larger than the average cell width $b$ of the tissue. Furthermore, although
555 the previous approximation of the tissue as formed by wedge-shaped cells no longer applies
556 to the whole tissue once extrusion begins, we may use it to approximate only the basal-most
557 layer of cells, for which the main effect of extrusion is to reduce the cellular density, that is,
558 to increase $b$. If extrusion eventually stops and the tissue reaches a new stable state, then the
559 average cell in the basalmost layer should reach an expected final width greater than ${b_0}^{PMA}$.
560 In this simplified explanation, both the occurrence and the extent to which cell extrusion
561 happens should be mainly determined by the relative decrease in the value of $T_a/T_0$ due to
562 PMA treatment, a consequence of the approximate power-law structure of the stability
563 threshold.

564 When extrapolating these observations to the living tissue, we could assimilate polarized
565 changes in surface tension to alterations in cell polarization (Moazzeni et al., 2025; Narayanan
566 et al., 2023). Treatment with PMA causes a loss of apico-basal cell polarity, evidenced by a
567 redistribution of the apical marker ZO-1, as well as of actin filaments. As expected, there was
568 also a re-localization of the main PKC substrate MARCKS, previously shown to be in great part
569 responsible for PMA-induced cell polarity downregulation and cell extrusion in the chick
570 neural plate (Aparicio et al., 2018). Evidence from this previous work also indicated that the
571 PMA effect on these cells could involve a destabilization of cortical actin filaments, probably
572 leading to a general reduction in cell surface tension (Chugh et al., 2017). This cortical actin
573 destabilization could be explained by an alteration in MARCKS function owed to its
574 phosphorylation at the effector domain by PKC, blocking its ability of sequestering $PIP_2$ at the
575 plasma membrane (Laux et al., 2000). Different lines of evidence have linked MARCKS to the
576 modulation of epithelial cell mechanical stability, and its involvement in processes such as

577 morphogenesis and carcinogenesis (Veloz et al., 2021). All the mentioned experimental
578 evidence points to an effect of PMA mostly on apical membrane tension, given the high apical
579 accumulation of MARCKS and actin filaments in neural plate cells, and that the basal
580 membrane domain is tightly associated to a rigid external scaffold, the basal lamina.

581 In summary, we have presented here evidence of the occurrence of live cell extrusion in the
582 neuroepithelium during neurulation, which could be caused by a reduction in cortical actin
583 cytoskeleton integrity and a concomitant down-regulation of apico-basal cell polarity. In order
584 to find a way of explaining these results within a mechanical framework, we have introduced
585 an expanded energy-based vertex model allowing for the presence of nuclei and curved
586 interfaces which is able to represent pseudostratified epithelial morphology. In line with
587 previous research, our work points to a high relative apical/basal surface tension as being the
588 main stabilizing factor against cell extrusion in high-density tissues such as the developing
589 neural plate. Furthermore, we derive a novel approximate condition for live cell extrusion
590 relating cell density and surface tension, which follows a power-law equation. Measurements
591 of surface tensions and cell densities in the developing neural plate could help validate these
592 results and contrast our approximation with other similar pre-existing models.
593
594
595
596
597
598
599
600
601
602
603
604
605

**Acknowledgements**

The authors gratefully acknowledge Dr. Lilián Perdomo and Prodhin SA for providing the fertilized hen eggs, and the Advanced Bioimaging Unit at the Institut Pasteur Montevideo for their support and assistance with microscopy. We thank Gonzalo Aparicio for initial help with chick embryo manipulation and fruitful discussion on the experimental aspects.

**Author contributions**

SABR: Conceptualization, Data curation, Formal analysis, Investigation, Methodology, Software, Writing – original draft, Writing – review and editing; JAH: Conceptualization, Formal analysis, Methodology, Supervision, Writing – review and editing; FRZ: Conceptualization, Data curation, Formal analysis, Funding acquisition, Methodology, Project administration, Resources, Supervision, Writing – original draft, Writing – review and editing.

**Funding sources**

This work was funded by CSIC-UdelaR grant C125-347 to FRZ; CAP-UdelaR Master's Fellowship to SABR; Dedicación Total-UdelaR, to FRZ; PEDECIBA.

**Conflict of interest:** The authors declare no conflict of interest.

**Data availability statement:** Original data and custom scripts written for GNU Octave are available at: Bosch, Santiago; Hernandez, Julio; Zolessi, Flavio (2025), "Data for "Mechanical conditions preventing live cell extrusion during primary neurulation in amniotes"", Mendeley Data, V1, doi: 10.17632/pc7ytf2xt7.1. Other data and materials are available from the corresponding author upon reasonable request.

630 **References**


631 Alvarez, I.S., Schoenwolf, G.C., 1992. Expansion of surface epithelium provides the major
632 extrinsic force for bending of the neural plate. J. Exp. Zool. 261, 340–348.
633 https://doi.org/10.1002/jez.1402610313

634 Ambrosini, A., Rayer, M., Monier, B., Suzanne, M., 2019. Mechanical Function of the Nucleus
635 in Force Generation during Epithelial Morphogenesis. Dev. Cell 50, 197-211.e5.
636 https://doi.org/10.1016/j.devcel.2019.05.027

637 Ampartzidis, I., Efstathiou, C., Paonessa, F., Thompson, E.M., Wilson, T., McCann, C.J., Greene,
638 N.De., Copp, A.J., Livesey, F.J., Elvassore, N., Giobbe, G.G., De Coppi, P., Maniou, E.,
639 Galea, G.L., 2023. Synchronisation of apical constriction and cell cycle progression is a
640 conserved behaviour of pseudostratified neuroepithelia informed by their tissue
641 geometry. Dev. Biol. 494, 60–70. https://doi.org/10.1016/j.ydbio.2022.12.002

642 Aparicio, G., Arruti, C., Zolessi, F.R., 2018. MARCKS phosphorylation by PKC strongly impairs
643 cell polarity in the chick neural plate. genesis 56, e23104.
644 https://doi.org/10.1002/dvg.23104

645 Arbuzova, A., Schmitz, A.A.P., Vergères, G., 2002. Cross-talk unfolded: MARCKS proteins.
646 Biochem. J. 362, 1–12. https://doi.org/10.1042/0264-6021:3620001

647 Atieh, Y., Wyatt, T., Zaske, A.M., Eisenhoffer, G.T., 2021. Pulsatile contractions promote
648 apoptotic cell extrusion in epithelial tissues. Curr. Biol. 31, 1129-1140.e4.
649 https://doi.org/10.1016/j.cub.2020.12.005

650 Campàs, O., Noordstra, I., Yap, A.S., 2024. Adherens junctions as molecular regulators of
651 emergent tissue mechanics. Nat. Rev. Mol. Cell Biol. 25, 252–269.
652 https://doi.org/10.1038/s41580-023-00688-7

653 Cearns, M.D., Escuin, S., Alexandre, P., Greene, N.D.E., Copp, A.J., 2016. Microtubules, polarity
654 and vertebrate neural tube morphogenesis. J. Anat. 229, 63–74.
655 https://doi.org/10.1111/joa.12468

656 Chapman, S.C., Collignon, J., Schoenwolf, G.C., Lumsden, A., 2001. Improved method for chick
657 whole-embryo culture using a filter paper carrier. Dev. Dyn. 220, 284–289.
658 https://doi.org/10.1002/1097-0177(20010301)220:3<284::AID-DVDY1102>3.0.CO;2-
659 5

660 Chen, J., Chang, S., Duncan, S.A., Okano, H.J., Fishell, G., Aderem, A., 1996. Disruption of the
661 MacMARCKS gene prevents cranial neural tube closure and results in anencephaly.

662 Proc. Natl. Acad. Sci. U. S. A. 93, 6275–6279. https://doi.org/10.1073/pnas.93.13.6275
663 Chugh, P., Clark, A.G., Smith, M.B., Cassani, D.A.D., Dierkes, K., Ragab, A., Roux, P.P., Charras,
664 G., Salbreux, G., Paluch, E.K., 2017. Actin cortex architecture regulates cell surface
665 tension. Nat. Cell Biol. 19, 689–697. https://doi.org/10.1038/ncb3525
666 Colas, J., Schoenwolf, G.C., 2001. Towards a cellular and molecular understanding of
667 neurulation. Dev. Dyn. 221, 117–145. https://doi.org/10.1002/dvdy.1144
668 Copp, A.J., Greene, N.D.E., 2010. Genetics and development of neural tube defects. J. Pathol.
669 220, 217–230. https://doi.org/10.1002/path.2643
670 de Goederen, V., Vetter, R., McDole, K., Iber, D., 2022. Hinge point emergence in mammalian
671 spinal neurulation. Proc. Natl. Acad. Sci. 119, e2117075119.
672 https://doi.org/10.1073/pnas.2117075119
673 de Leeuw, N.F., Budhathoki, R., Russell, L.J., Loerke, D., Blankenship, J.T., 2024. Nuclei as
674 mechanical bumpers during epithelial remodeling. J. Cell Biol. 223, e202405078.
675 https://doi.org/10.1083/jcb.202405078
676 Drozdowski, O.M., Schwarz, U.S., 2024. Cell bulging and extrusion in a three-dimensional
677 bubbly vertex model for curved epithelial sheets.
678 https://doi.org/10.48550/arXiv.2411.07141
679 Duclut, C., Paijmans, J., Inamdar, M.M., Modes, C.D., Jülicher, F., 2021. Nonlinear rheology of
680 cellular networks. Cells Dev. 168, 203746.
681 https://doi.org/10.1016/j.cdev.2021.203746
682 Duszyc, K., Gomez, G.A., Lagendijk, A.K., Yau, M.K., Nanavati, B.N., Gliddon, B.L., Hall, T.E.,
683 Verma, S., Hogan, B.M., Pitson, S.M., Fairlie, D.P., Parton, R.G., Yap, A.S., 2021.
684 Mechanotransduction activates RhoA in the neighbors of apoptotic epithelial cells to
685 engage apical extrusion. Curr. Biol. 31, 1326-1336.e5.
686 https://doi.org/10.1016/j.cub.2021.01.003
687 Eaton, J.W., Bateman, D., Hauberg, S., Wehbring, R., 2020. GNU Octave version 6.1.0 manual:
688 a high-level interactive language for numerical computations. [WWW Document].
689 URL https://www.gnu.org/software/octave/doc/v6.1.0/
690 Eisenhoffer, G.T., Loftus, P.D., Yoshigi, M., Otsuna, H., Chien, C.-B., Morcos, P.A., Rosenblatt,
691 J., 2012. Crowding induces live cell extrusion to maintain homeostatic cell numbers in
692 epithelia. Nature 484, 546–549. https://doi.org/10.1038/nature10999
693 Eisenhoffer, G.T., Rosenblatt, J., 2013. Bringing balance by force: live cell extrusion controls

694 epithelial cell numbers. Trends Cell Biol. 23, 185–192.
695 https://doi.org/10.1016/j.tcb.2012.11.006
696 El Amri, M., Fitzgerald, U., Schlosser, G., 2018. MARCKS and MARCKS-like proteins in
697 development and regeneration. J. Biomed. Sci. 25, 43.
698 https://doi.org/10.1186/s12929-018-0445-1
699 Escuin, S., Vernay, B., Savery, D., Gurniak, C.B., Witke, W., Greene, N.D.E., Copp, A.J., 2015.
700 Rho-kinase-dependent actin turnover and actomyosin disassembly are necessary for
701 mouse spinal neural tube closure. J. Cell Sci. 128, 2468–2481.
702 https://doi.org/10.1242/jcs.164574
703 Ferme, L.C., Ryan, A.Q., Haase, R., Modes, C.D., Norden, C., 2025. Timely neurogenesis drives
704 the transition from nematic to crystalline nuclear packing during retinal
705 morphogenesis. Sci. Adv. 11, eadu6843. https://doi.org/10.1126/sciadv.adu6843
706 Gómez, H.F., Dumond, M.S., Hodel, L., Vetter, R., Iber, D., 2021. 3D cell neighbour dynamics
707 in growing pseudostratified epithelia. eLife 10, e68135.
708 https://doi.org/10.7554/eLife.68135
709 Hamburger, V., Hamilton, H.L., 1951. A series of normal stages in the development of the chick
710 embryo. J. Morphol. 88, 49–92. https://doi.org/10.1002/jmor.1050880104
711 Hecht, S., Perez-Mockus, G., Schienstock, D., Recasens-Alvarez, C., Merino-Aceituno, S.,
712 Smith, M.B., Salbreux, G., Degond, P., Vincent, J.-P., 2022. Mechanical constraints to
713 cell-cycle progression in a pseudostratified epithelium. Curr. Biol. 32, 2076-2083.e2.
714 https://doi.org/10.1016/j.cub.2022.03.004
715 Iber, D., Vetter, R., 2022. 3D Organisation of Cells in Pseudostratified Epithelia. Front. Phys.
716 10, 898160. https://doi.org/10.3389/fphy.2022.898160
717 Ishii, M., Tateya, T., Matsuda, M., Hirashima, T., 2021. Stalling interkinetic nuclear migration
718 in curved pseudostratified epithelium of developing cochlea. R. Soc. Open Sci. 8,
719 211024. https://doi.org/10.1098/rsos.211024
720 Kalukula, Y., Stephens, A.D., Lammerding, J., Gabriele, S., 2022. Mechanics and functional
721 consequences of nuclear deformations. Nat. Rev. Mol. Cell Biol. 23, 583–602.
722 https://doi.org/10.1038/s41580-022-00480-z
723 Kim, S., Amini, R., Yen, S.-T., Pospíšil, P., Boutillon, A., Deniz, I.A., Campàs, O., 2024. A nuclear
724 jamming transition in vertebrate organogenesis. Nat. Mater. 23, 1592–1599.
725 https://doi.org/10.1038/s41563-024-01972-3

726 Kim, S., Pochitaloff, M., Stooke-Vaughan, G.A., Campàs, O., 2021. Embryonic tissues as active
727 foams. Nat. Phys. 17, 859–866. https://doi.org/10.1038/s41567-021-01215-1
728 Laux, T., Fukami, K., Thelen, M., Golub, T., Frey, D., Caroni, P., 2000. GAP43, MARCKS, and
729 CAP23 modulate PI(4,5)P(2) at plasmalemmal rafts, and regulate cell cortex actin
730 dynamics through a common mechanism. J. Cell Biol. 149, 1455–1472.
731 https://doi.org/10.1083/jcb.149.7.1455
732 Lee, H., Nagele, R.G., 1988. Intrinsic forces alone are sufficient to cause closure of the neural
733 tube in the chick. Experientia 44, 60–61. https://doi.org/10.1007/BF01960246
734 Lubkov, V., Bar-Sagi, D., 2014. E-Cadherin-Mediated Cell Coupling Is Required for Apoptotic
735 Cell Extrusion. Curr. Biol. 24, 868–874. https://doi.org/10.1016/j.cub.2014.02.057
736 Madara, J.L., 1990. Maintenance of the macromolecular barrier at cell extrusion sites in
737 intestinal epithelium: Physiological rearrangement of tight junctions. J. Membr. Biol.
738 116, 177–184. https://doi.org/10.1007/BF01868675
739 Marinari, E., Mehonic, A., Curran, S., Gale, J., Duke, T., Baum, B., 2012. Live-cell delamination
740 counterbalances epithelial growth to limit tissue overcrowding. Nature 484, 542–545.
741 https://doi.org/10.1038/nature10984
742 Martin, A.C., Goldstein, B., 2014. Apical constriction: themes and variations on a cellular
743 mechanism driving morphogenesis. Development 141, 1987–1998.
744 https://doi.org/10.1242/dev.102228
745 McLaughlin, S., Aderem, A., 1995. The myristoyl-electrostatic switch: a modulator of
746 reversible protein-membrane interactions. Trends Biochem. Sci. 20, 272–276.
747 https://doi.org/10.1016/s0968-0004(00)89042-8
748 Moazzeni, S., Kyker-Snowman, K., Cohen, R.I., Wang, H., Li, R., Shreiber, D.I., Zahn, J.D., Shi,
749 Z., Lin, H., 2025. N-Cadherin based adhesion and Rac1 activity regulate tension
750 polarization in the actin cortex. Sci. Rep. 15, 4296. https://doi.org/10.1038/s41598-
751 025-88537-9
752 Moury, J.D., Schoenwolf, G.C., 1995. Cooperative model of epithelial shaping and bending
753 during avian neurulation: autonomous movements of the neural plate, autonomous
754 movements of the epidermis, and interactions in the neural plate/epidermis transition
755 zone. Dev. Dyn. 204, 323–337. https://doi.org/10.1002/aja.1002040310
756 Nanavati, B.N., Yap, A.S., Teo, J.L., 2020. Symmetry Breaking and Epithelial Cell Extrusion. Cells
757 9, 1416. https://doi.org/10.3390/cells9061416

758 Narayanan, V., Purkayastha, P., Yu, B., Pendyala, K., Chukkapalli, S., Cabe, J.I., Dickinson, R.B.,
759 Conway, D.E., Lele, T.P., 2023. Rho activation drives luminal collapse and eversion in
760 epithelial acini. Biophys. J. 122, 3630–3645.
761 https://doi.org/10.1016/j.bpj.2023.01.005
762 Norden, C., 2017. Pseudostratified epithelia - cell biology, diversity and roles in organ
763 formation at a glance. J. Cell Sci. 130, 1859–1863. https://doi.org/10.1242/jcs.192997
764 Odell, G.M., Oster, G., Alberch, P., Burnside, B., 1981. The mechanical basis of morphogenesis.
765 I. Epithelial folding and invagination. Dev. Biol. 85, 446–462.
766 https://doi.org/10.1016/0012-1606(81)90276-1
767 Okuda, H., Kuwahara, R., Matsuzaki, S., Miyata, S., Kumamoto, N., Hattori, T., Shimizu, S.,
768 Yamada, K., Kawamoto, K., Hashimoto, R., Takeda, M., Katayama, T., Tohyama, M.,
769 2010. Dysbindin regulates the transcriptional level of myristoylated alanine-rich
770 protein kinase C substrate via the interaction with NF-YB in mice brain. PloS One 5,
771 e8773. https://doi.org/10.1371/journal.pone.0008773
772 Prieto, D., Zolessi, F.R., 2017. Functional Diversification of the Four MARCKS Family Members
773 in Zebrafish Neural Development. J. Exp. Zoolog. B Mol. Dev. Evol. 328, 119–138.
774 https://doi.org/10.1002/jez.b.22691
775 Roby, N., Rauzi, M., 2025. Nuclear position controls the activity of cortical actomyosin
776 networks powering simultaneous morphogenetic events. Nat. Commun. 16, 1587.
777 https://doi.org/10.1038/s41467-025-56880-0
778 Roellig, D., Theis, S., Proag, A., Allio, G., Bénazéraf, B., Gros, J., Suzanne, M., 2022. Force-
779 generating apoptotic cells orchestrate avian neural tube bending. Dev. Cell 57, 707-
780 718.e6. https://doi.org/10.1016/j.devcel.2022.02.020
781 Rosenblatt, J., Raff, M.C., Cramer, L.P., 2001. An epithelial cell destined for apoptosis signals
782 its neighbors to extrude it by an actin- and myosin-dependent mechanism. Curr. Biol.
783 11, 1847–1857. https://doi.org/10.1016/S0960-9822(01)00587-5
784 Saade, M., Martí, E., 2025. Early spinal cord development: from neural tube formation to
785 neurogenesis. Nat. Rev. Neurosci. 26, 195–213. https://doi.org/10.1038/s41583-025-
786 00906-5
787 Sauer, F.C., 1936. The interkinetic migration of embryonic epithelial nuclei. J. Morphol. 60, 1–
788 11. https://doi.org/10.1002/jmor.1050600102
789 Saw, T.B., Doostmohammadi, A., Nier, V., Kocgozlu, L., Thampi, S., Toyama, Y., Marcq, P., Lim,

790 C.T., Yeomans, J.M., Ladoux, B., 2017. Topological defects in epithelia govern cell
791 death and extrusion. Nature 544, 212–216. https://doi.org/10.1038/nature21718
792 Sawyer, J.K., Choi, W., Jung, K.C., He, L., Harris, N.J., Peifer, M., 2011. A contractile actomyosin
793 network linked to adherens junctions by Canoe/afadin helps drive convergent
794 extension. Mol. Biol. Cell 22, 2491–2508. https://doi.org/10.1091/mbc.E11-05-0411
795 Schindelin, J., Arganda-Carreras, I., Frise, E., Kaynig, V., Longair, M., Pietzsch, T., Preibisch, S.,
796 Rueden, C., Saalfeld, S., Schmid, B., Tinevez, J.-Y., White, D.J., Hartenstein, V., Eliceiri,
797 K., Tomancak, P., Cardona, A., 2012. Fiji: an open-source platform for biological-image
798 analysis. Nat. Methods 9, 676–682. https://doi.org/10.1038/nmeth.2019
799 Schoenwolf, G.C., 2018. Contributions of the chick embryo and experimental embryology to
800 understanding the cellular mechanisms of neurulation. Int. J. Dev. Biol. 62, 49–55.
801 https://doi.org/10.1387/ijdb.170288gs
802 Schoenwolf, G.C., Powers, M.L., 1987. Shaping of the chick neuroepithelium during primary
803 and secondary neurulation: Role of cell elongation. Anat. Rec. 218, 182–195.
804 https://doi.org/10.1002/ar.1092180214
805 Schoenwolf, G.C., Smith, J.L., 1990. Mechanisms of neurulation: traditional viewpoint and
806 recent advances. Dev. Camb. Engl. 109, 243–270.
807 https://doi.org/10.1242/dev.109.2.243
808 Slattum, G.M., Rosenblatt, J., 2014. Tumour cell invasion: an emerging role for basal epithelial
809 cell extrusion. Nat. Rev. Cancer 14, 495–501. https://doi.org/10.1038/nrc3767
810 Sluysmans, S., Vasileva, E., Spadaro, D., Shah, J., Rouaud, F., Citi, S., 2017. The role of apical
811 cell-cell junctions and associated cytoskeleton in mechanotransduction. Biol. Cell 109,
812 139–161. https://doi.org/10.1111/boc.201600075
813 Smith, J.L., Schoenwolf, G.C., 1988. Role of cell-cycle in regulating neuroepithelial cell shape
814 during bending of the chick neural plate. Cell Tissue Res. 252, 491–500.
815 https://doi.org/10.1007/BF00216636
816 Stern, C.D., Holland, P.W.H. (Eds.), 1993. Essential Developmental Biology: A Practical
817 Approach. Oxford University Press.
818 https://doi.org/10.1093/oso/9780199634231.001.0001
819 Stumpo, D.J., Bock, C.B., Tuttle, J.S., Blackshear, P.J., 1995. MARCKS deficiency in mice leads
820 to abnormal brain development and perinatal death. Proc. Natl. Acad. Sci. U. S. A. 92,
821 944–948. https://doi.org/10.1073/pnas.92.4.944

822 Tanimura, N., Fujita, Y., 2020. Epithelial defense against cancer (EDAC). Semin. Cancer Biol.
823 63, 44–48. https://doi.org/10.1016/j.semcancer.2019.05.011
824 Toledo, A., Zolessi, F.R., Arruti, C., 2013. A novel effect of MARCKS phosphorylation by
825 activated PKC: the dephosphorylation of its serine 25 in chick neuroblasts. PloS One 8,
826 e62863. https://doi.org/10.1371/journal.pone.0062863
827 Veloz, L., Bosch, S., Aparicio, G., Zolessi, F., 2021. Cell extrusion in development and cancer,
828 what MARCKS the difference for epithelial integrity? BIOCELL 46, 639–644.
829 https://doi.org/10.32604/biocell.2022.018798
830 Zhang, L., Wei, X., 2025. The Lego hypothesis of tissue morphogenesis: stereotypic
831 organization of parallel orientational cell adhesions for epithelial self-assembly. Biol.
832 Rev. Camb. Philos. Soc. 100, 445–460. https://doi.org/10.1111/brv.13147
833 Zolessi, F.R., Arruti, C., 2001. Apical accumulation of MARCKS in neural plate cells during
834 neurulation in the chick embryo. BMC Dev. Biol. 1, 7. https://doi.org/10.1186/1471-
835 213X-1-7
836
837

838 **Figure 1: Diagram of terms included in the energy equation of our model.** Here the vertices
839 defining the boundary of cell i are represented along with its nucleus and its neighboring cells,
840 similar to our simulation results. The first energy term in Eq. 1 depends on interface length
841 $L_{ij}$ which depends on the cells involved in the interface (e.g.: ij, ik, ig, as shown here). Apical
842 and basal surfaces are here composed of yellow and orange vertices, with lengths marked as
843 $L_i^a$ and $L_i^b$ respectively. The third term in Eq. 1 corresponds to interactions with the nuclei and
844 depends, for every point in the cell boundary, on its distance from the nuclear center $r_i$ and
845 on $R_i$, the "radius" of the nucleus in the same direction. Note that this third term is only non-
846 zero when $R_i > r_i$, i.e.: when the nucleus overlaps the cell boundary.
847
848 **Figure 2: Comparison of chick embryos after treatment with PMA and QVD-OPh**. **A.**
849 Macroscopic view of treated embryos. Embryos treated with the pan-anti-caspase drug QVD-
850 OPh seemed to develop similarly to Control embryos. Those treated with PMA, both alone
851 and together with QVD-OPh, showed several defects, as described previously (Aparicio et al.,
852 2018), including decreased length, neural tube closure failure and abnormally open anterior
853 (filled arrowheads) and posterior (hollow arrowheads) neuropores. Scalebar: 1 mm. **B.**
854 Transverse sections of the neural plate and adjacent tissues. Control and QVD-OPh-treated
855 embryos displayed a thick pseudostratified epithelium. Treatment with PMA (including
856 double treatment with QVD-OPh) produced widespread apical cell extrusion, evidenced by
857 the presence of cells beyond the line of F-actin accumulation (dashed line; corresponding to
858 the apical side of the layer of cells attached to the basal lamina), which are present along all
859 regions of the neural plate. Scalebar: 50 µm
860
861 **Figure 3: Distribution of MARCKS and ZO-1 along the apico-basal axis of the**
862 **neuroepithelium.** Intracellular distribution of MARCKS (**A**) and ZO-1 (**B**) in different
863 experimental conditions. Both proteins accumulate near the apical side in control embryos,
864 but have seemingly altered distributions under PMA and PMA + QVD-OPh double treatment,
865 sometimes even presenting anomalous accumulations away from the line of F-actin
866 accumulation (arrowheads). **C**. Example of intensity profiles used to determine the
867 fluorescence intensity around the apical border (in gray; defined as the area of maximal F-
868 actin accumulation) and along the sub-apical portion of the neuroepithelium in different

869 conditions (only control condition example is shown). **D**. Plots for the ratio of the maximum
870 immunofluorescent signal intensity in the apical regions relative to the average signal
871 intensity of the sub-apical region for both proteins. Data shows significant differences
872 between the geometric mean values for PMA-treated embryos with respect to Control (p-
873 values = 0.0416 (ZO-1); 0.0279 (MARCKS)) and QVD-OPh-treated embryos (p-values = 0.0044
874 (ZO-1); <0.0001 (MARCKS)), and between QVD-OPh- and double-treatment embryos (p-
875 values = 0.0233 (ZO-1); 0.0390 (MARCKS), indicating altered apico-basal polarity. Data are
876 presented along with geometric mean and geometric standard deviation.

877

878 **Figure 4: Occurrence of cell death among different experimental conditions. A**. Examples
879 taken from slices of embryos treated with PMA or PMA + QVD-OPh, illustrating the
880 differences in signs of cell death. In PMA-treated embryos cells undergoing cell death were
881 often observed, as indicated by the presence of pyknotic nuclei and/or caspase-3 activity
882 (arrowheads). **B**. The number of pyknotic nuclei and cells displaying active caspase-3
883 immunodetection was higher in PMA-treated embryos than in all other experimental
884 conditions. Most notably, double treatment with PMA and QVD-OPh abolished cell death
885 while still inducing widespread cell extrusion. The dashed line marks the line of F-actin
886 accumulation, corresponding to the apical side of the layer of cells attached to the basal
887 lamina. Filled arrowheads: Cells exhibiting both pyknotic nuclei and active caspase-3. Hollow
888 arrowhead: A cell with a pyknotic nucleus but no active caspase-3 immunoreactivity. Data
889 presented along with median and 95% confidence interval.

890

891 **Figure 5: Dynamic simulations of pseudostratified epithelia including nuclei, using the**
892 **energy model. A.** Diagram depicting the state of a typical system at time t as obtained by
893 dynamical simulation. Vertices are colored according to the type of interface they belong to
894 (cell-cell interfaces are blue, while apical and basal interfaces are orange and yellow,
895 respectively), and each cell contains a nucleus tagged according to the cell number. Periodic
896 boundary conditions are used in the x-axis. Both axes are taken to be relative to the
897 characteristic length scale $L_0 = \sqrt{A_0}$. **B**. Long-term behavior of dynamic simulations in tissues
898 with 20 cells, and an average cell width b = 0.5, under different values of $T_a/T_0$. All simulations
899 start from a layer of identical rectangular cells with area $A_0$ (= 1) and alternating nuclei, and

are left to run for 20 characteristic time-lengths ($\tau_R$). These initial and final states are marked as $t_0$ and $t_f$, respectively. Energy profiles indicated an apparent equilibrium state for all cases except for when $T_a/T_0 = 1.5$. For low values of $T_a/T_0$, a single layer morphology is unstable and cell extrusion ensues, while for larger values the single layer is maintained at equilibrium. For values larger than 5, a stable equilibrium solution resembling the pseudostratified epithelial morphology is reached. **C-E.** Simulations were performed at this stable value of $T_a/T_0 = 5$ for other nuclear configurations, all of which also proved stable in these conditions: a "staircase" distribution with intermediate nuclei (**C**) and different random nuclear distributions (**D**,**E**).

**Figure 6: Long-term stability analysis for a monolayer composed of identical alternating wedge-shaped cells with no nuclei in terms of tissue parameters. A**. To study the stability of a simple cell layer we consider an infinite tissue made up of alternating, identical wedge-shaped cells. The shape of one of these cells may be determined by its height ($h$) and its basal width ($b_b$), assuming that the apical and basal interfaces correspond to circular arcs and that cell-cell interfaces are straight. The width of any two adjacent cells adds up to double the average cell width $b$, which is the inverse of cellular density. For each set of parameters, we find the basal width and height that minimize the total tissue energy. **B.** Value of the basal width $b_b$ (expressed as a fraction of average cell width $b$) corresponding to the energy minimum vs $b$, here represented for different values of the ratio between apical/basal and lateral surface tension $T_a/T_0$. Although for low values of $T_a/T_0$ these graphs seem more complex, for values larger than 0.87, the plot of $b_b/b$ vs $b$ seems to be divided into three distinct ranges: a low range where $b_b = 0$, a middle range, and a high range where the energy minimum corresponds to $b_b = b$. Values $b_0$ and $b_1$ limit the low and high ranges for each $T_a/T_0$ (arrowheads). **C**. Plot of $b_0$ (blue dotted line) and $b_1$ (orange dotted line) as functions of $T_a/T_0$. For sufficiently large $T_a/T_0$, systems with parameters lying in the region above the $b_1$ curve have their energy minima when $b_b = b$ (epithelial stability) while those below $b_0$ tend to $b_b = 0$ at equilibrium, which leads to cell extrusion. C' shows the natural log-log plot of $b_0$ and $b_1$ vs. $T_a/T_0$. Fitted (dashed) lines correspond to equations $log(b_0) = -0.5612\, ln(T_a/T_0) - 0.4237$ and $log(b_1) = -0.5761 ln(T_a/T_0) - 0.3729$. When

930 simulations yielded values of $b_b/b$ larger than 1, they were replaced by $2 - b_b/b$, making use
931 of the tissue apico-basal symmetry.
932
933 **Figure 7: Comparison between dynamical simulations and stability predictions based on a**
934 **tissue composed of wedge-shaped cells.** Dynamical simulations like those of Fig. 5 were run
935 here based on the quantitative analysis shown in Fig. 6, in and around the area in which
936 wedge-shaped cells are expected in equilibrium, close to the stability threshold. **A**. Detail of
937 $b_0$ and $b_1$ as functions of $T_a/T_0$, showing points corresponding to the simulations shown in B-
938 F. Dashed gray lines point to the threshold value found for $T_a/T_0$ at $b = 0.5$. The dotted gray
939 line marks the calculated value of $b = 0.604$, above which there would be no cell extrusion.
940 **B**. Starting with nuclei distributed alternatingly and $b = 0.5$, we observe cell extrusion for
941 $T_a/T_0 = 1.5$ (see Supplementary Video 1). **C.** Also at $b = 0.5$, we can have many different
942 outcomes for variable initial nuclear positions, at a tension ratio value that is slightly higher
943 than the predicted threshold ($T_a/T_0 = 1.6$). When nuclei start in an alternated position like
944 in B or in a "staircase" distribution, cell extrusion is prevented (Supplementary Video 2).
945 Random nuclear distributions, on the other hand, resulted in cell extrusion, as shown in the
946 two bottom examples. **D.** In dynamical simulations with $b = 0.5$ and $T_a/T_0 = 0.55$, not only
947 did cell extrusion occur (contrary to our predictions) but also artefacts were introduced in the
948 form of overlapping cell boundaries (arrowheads; detail in inset). **E,F**. Lowering cell density to
949 16 cells ($b = 0.625$) means the system should lie above $b_0$ according to our approximation
950 regardless of surface tension. Although in these conditions and $T_a/T_0 = 0.55$ the cells adopt
951 a rounded morphology, with a great expansion of one of their external surfaces, there is no
952 cell extrusion (E). When the tension ratio was increased to $T_a/T_0 = 1$, cells adopted a less-
953 extreme wedge shape, also without extrusion as expected (F).
954

Figure 1

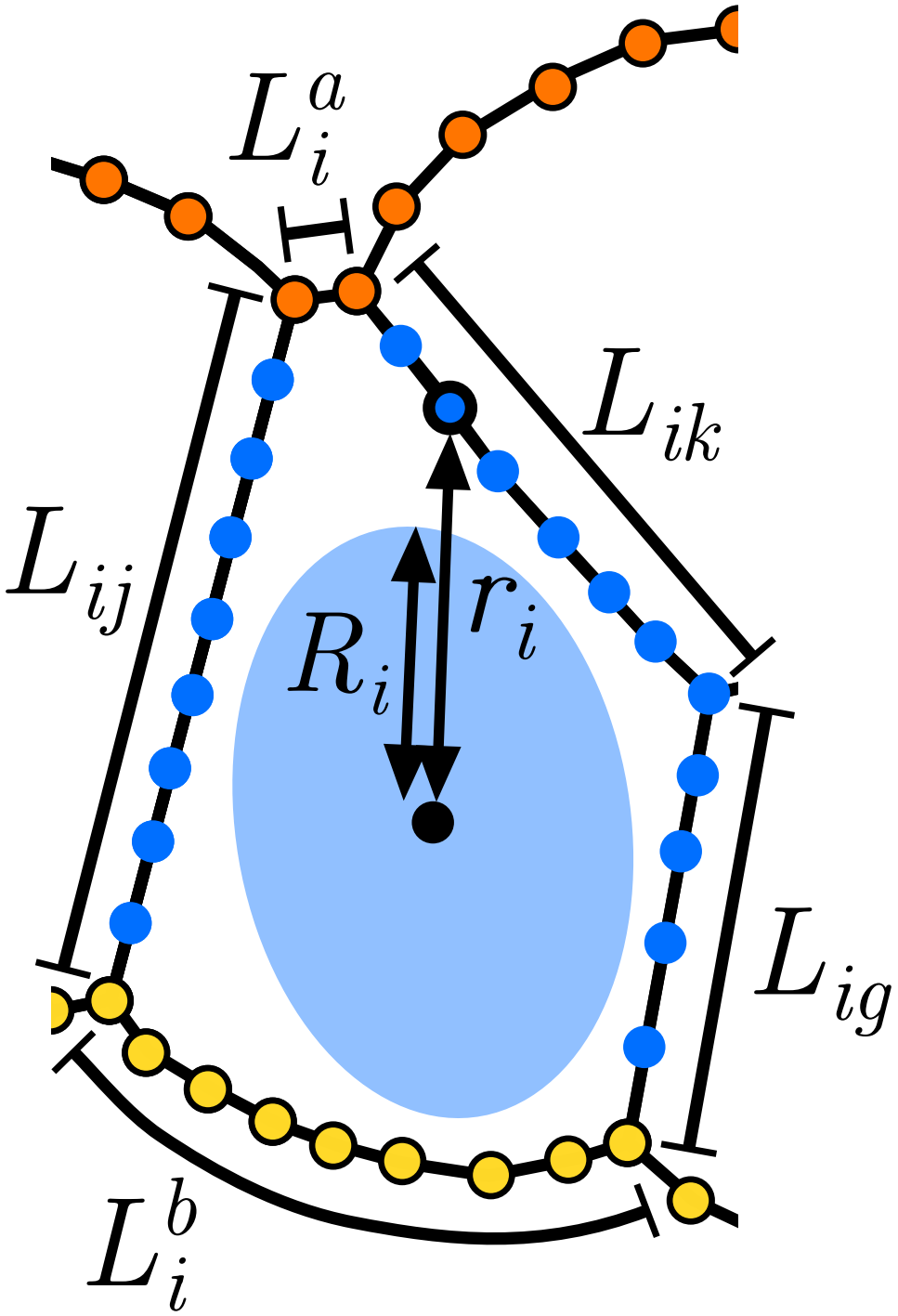

# Figure 2

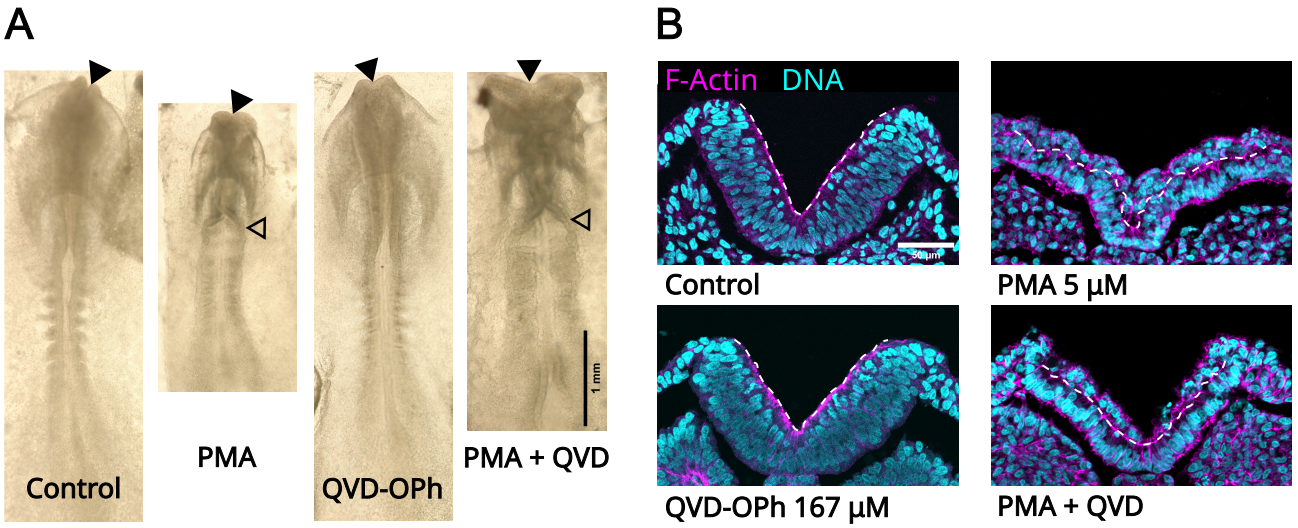
A
Control
PMA
QVD-OPh
PMA + QVD
1 mm
B
F-Actin
DNA
50 µm
Control
PMA 5 µM
QVD-OPh 167 µM
PMA + QVD

# Figure 3

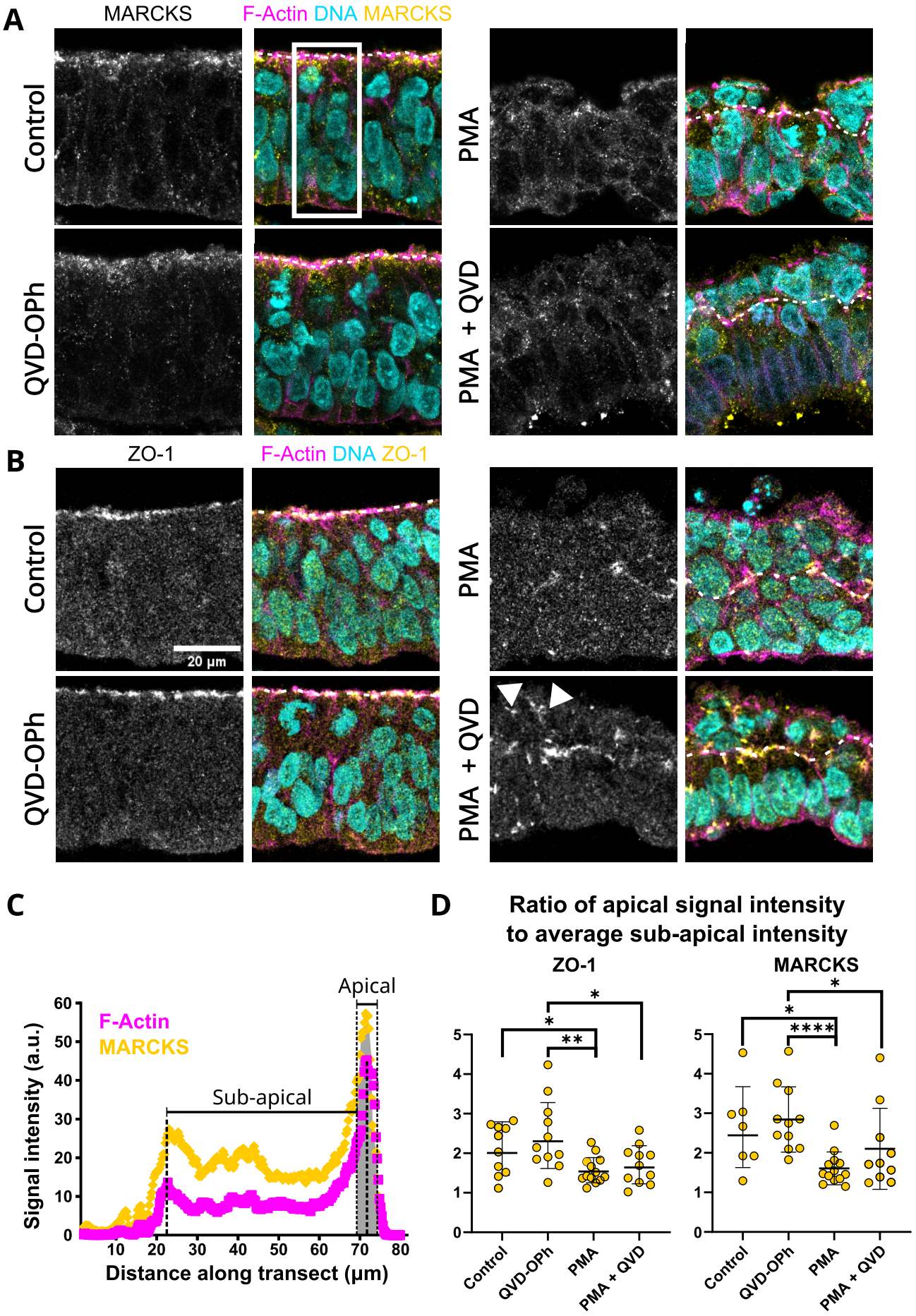
A
MARCKS
F-Actin DNA MARCKS
Control
QVD-OPh
PMA
PMA + QVD
B
ZO-1
F-Actin DNA ZO-1
20 µm
C
F-Actin
MARCKS
Apical
Sub-apical
Signal intensity (a.u.)
Distance along transect (µm)
D
Ratio of apical signal intensity
to average sub-apical intensity
ZO-1
MARCKS
Control
QVD-OPh
PMA
PMA + QVD

# Figure 4

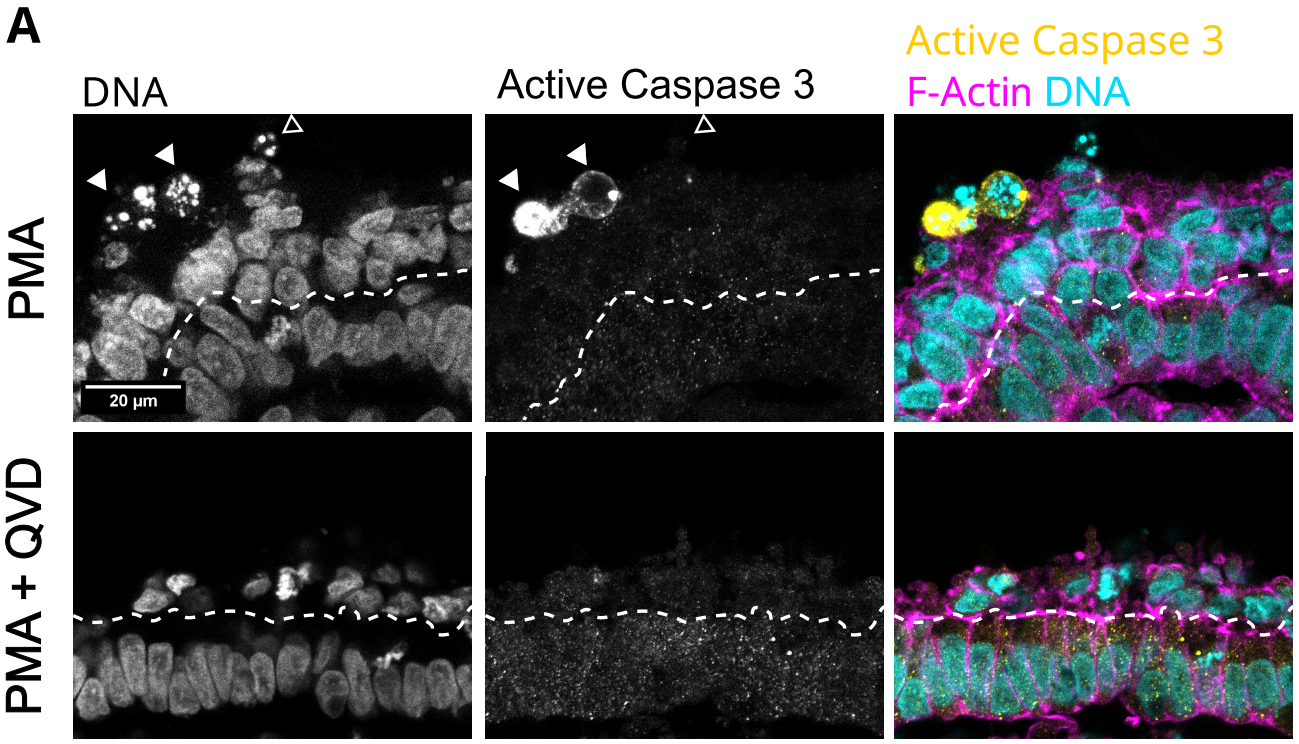
A
DNA
Active Caspase 3
Active Caspase 3
F-Actin DNA
PMA
PMA + QVD
20 µm

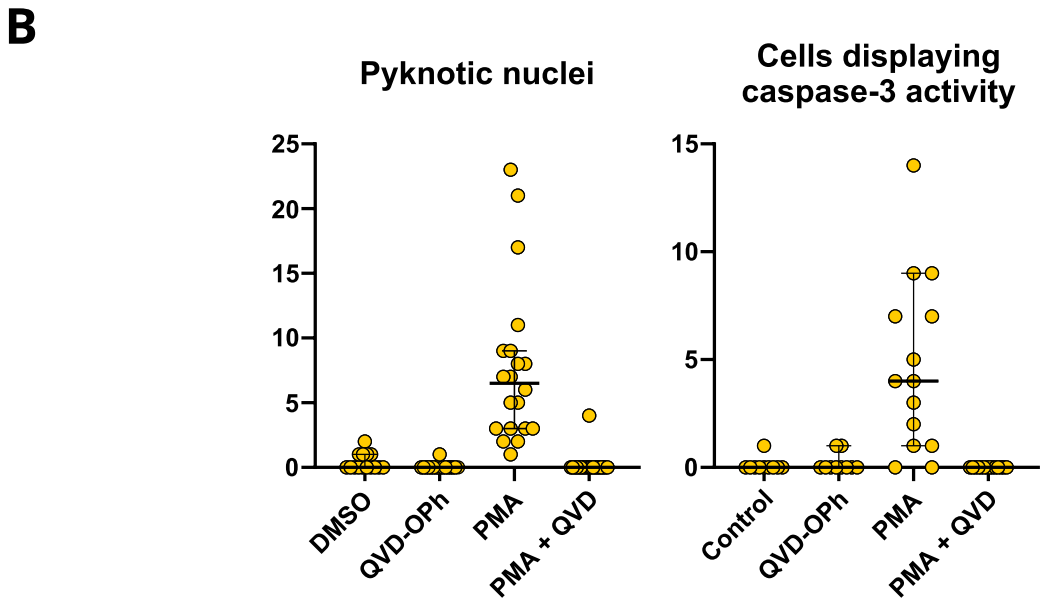
B
Pyknotic nuclei
Cells displaying caspase-3 activity
25
20
15
10
5
0
DMSO
QVD-OPh
PMA
PMA + QVD
15
10
5
0
Control
QVD-OPh
PMA
PMA + QVD

# Figure 5

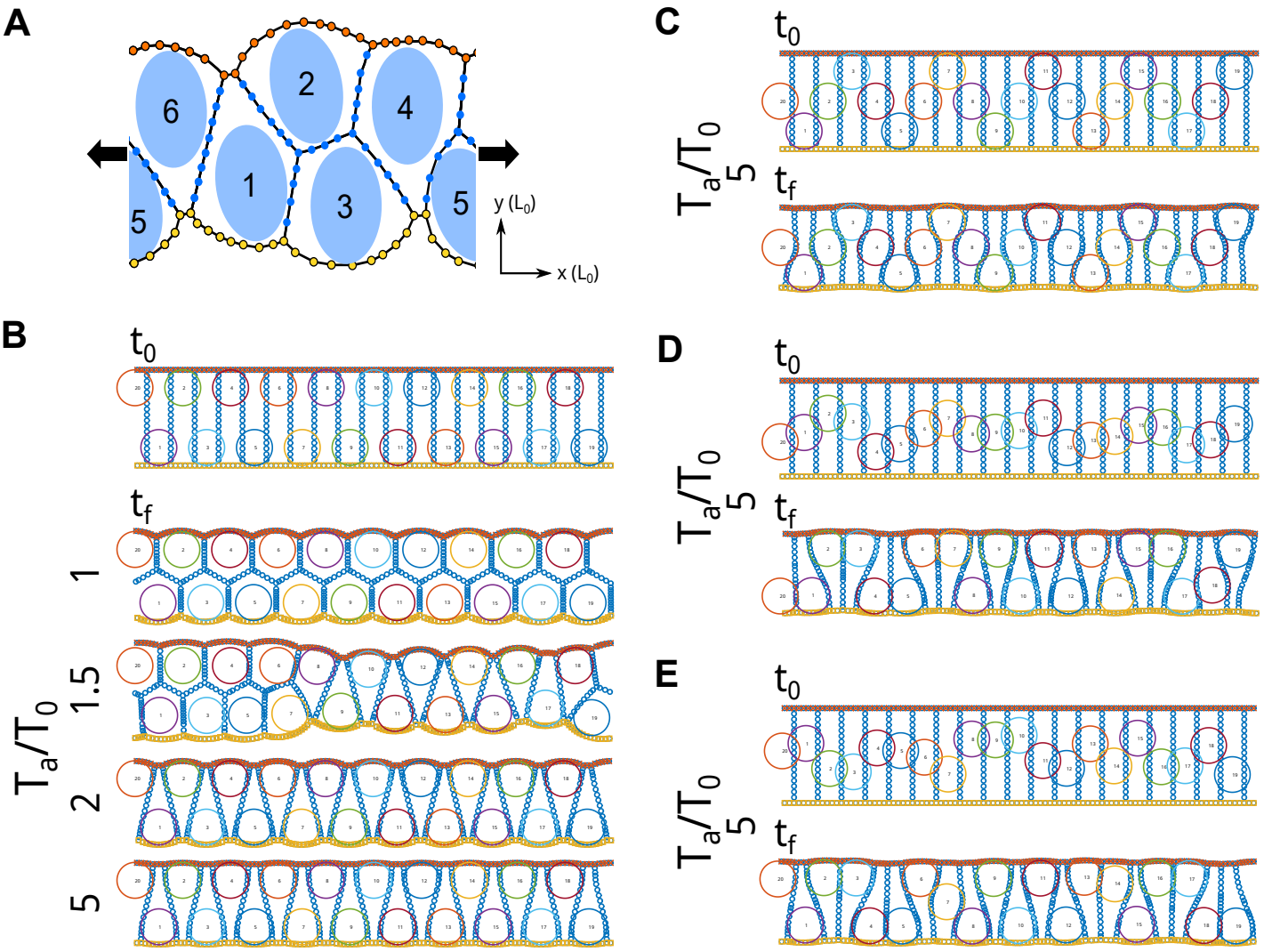
A
6
2
4
1
3
5
5
y (L0)
x (L0)
B
t0
tf
Ta/T0
1
1.5
2
5
C
t0
tf
Ta/T0
5
D
t0
tf
Ta/T0
5
E
t0
tf
Ta/T0
5

# Figure 6

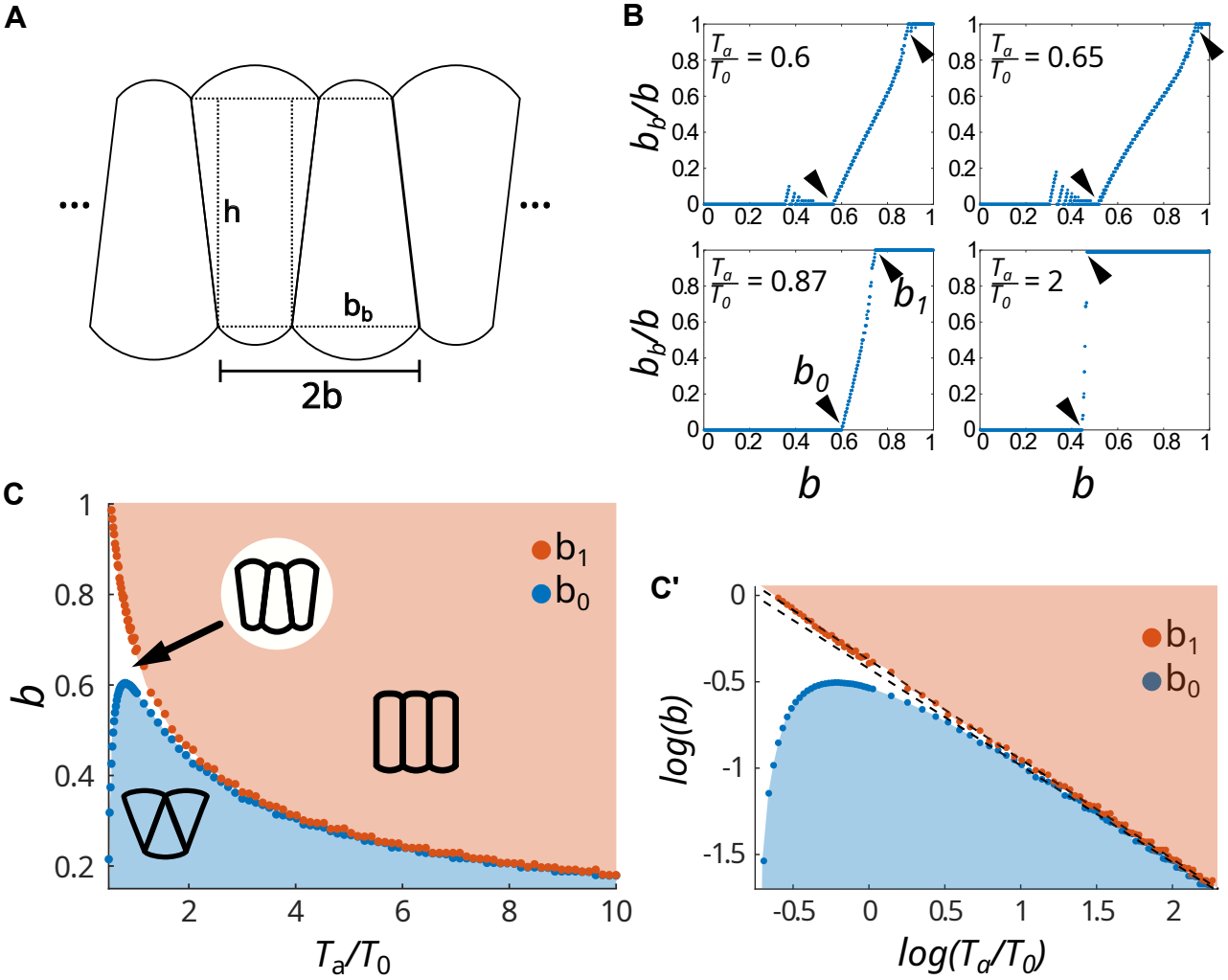
A
h
$b_b$
2b
B
$\frac{T_a}{T_0}$ = 0.6
$\frac{T_a}{T_0}$ = 0.65
$\frac{T_a}{T_0}$ = 0.87
$\frac{T_a}{T_0}$ = 2
$b_1$
$b_0$
$b_b/b$
b
C
$b_1$
$b_0$
b
$T_a/T_0$
C'
$b_1$
$b_0$
log(b)
$log(T_a/T_0)$

Figure 7

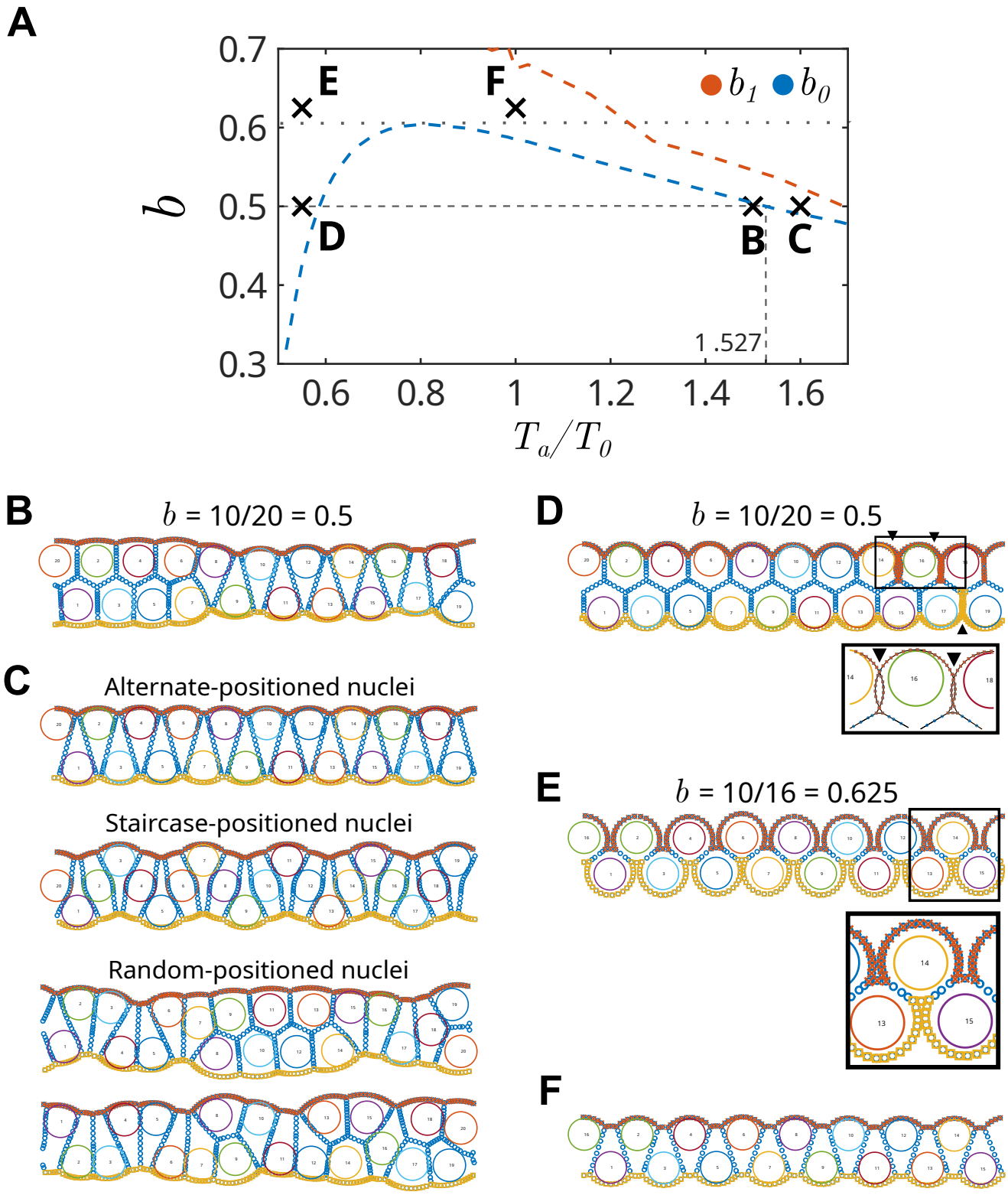
A
0.7
0.6
0.5
0.4
0.3
b
E
F
D
B
C
$b_1$
$b_0$
1 .527
0.6
0.8
1
1.2
1.4
1.6
$T_a/T_0$
B
$b$ = 10/20 = 0.5
C
Alternate-positioned nuclei
Staircase-positioned nuclei
Random-positioned nuclei
D
$b$ = 10/20 = 0.5
E
$b$ = 10/16 = 0.625
F

# Supplementary Figure 1

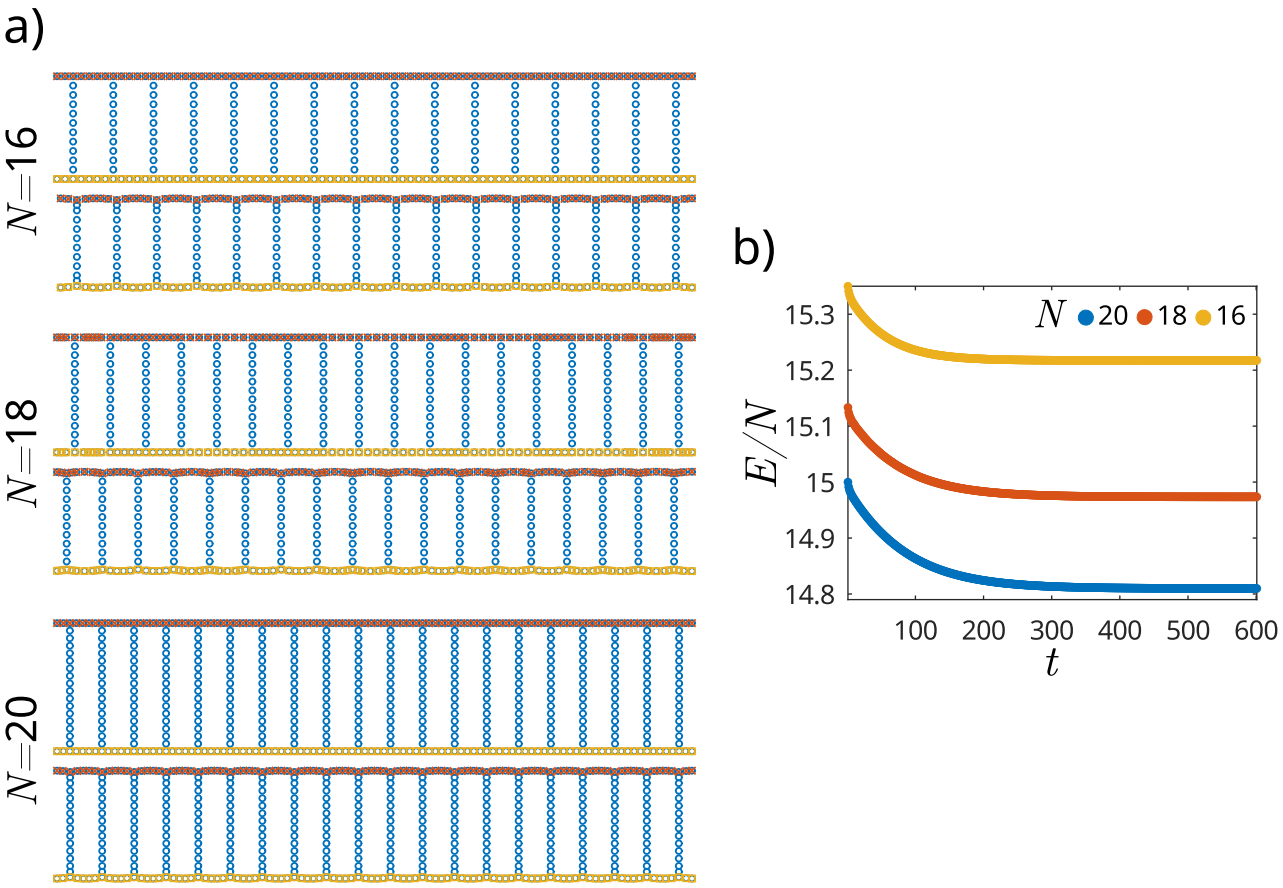


**Supplementary Figure 1: Initial simulations performed without nuclei quickly reach equilibrium in less than $2\tau_R$.** (A) Starting from an initial configuration of *N* identical rectangular cells with unit area, a stable state was reached composed of cells with straight cell-cell and convex cell-exterior interfaces, here pictured for *N = 16, 18, 20* after 400 integration steps (equivalent to twice the characteristic time for vertex relaxation). This state was achieved even when the initial vertex distribution was not homogeneous, as in the case of *N = 18*. (B) Plot of energy E per cell in time. Initial and final values were quantitatively similar for all cases, although the relaxation time became larger the smaller the average cell width b, with $t_{50}$ (the time required to lose half the total lost energy) being $0.165\tau_R$, $0.235\tau_R$ and $0.27\tau_R$ for *N = 16, 18* and *20* respectively. Here we continued the simulation until $3\tau_R$, but we can qualitatively see that the system has reached equilibrium before that. $T_a/T_0 = 3$ for all shown simulations.

# Supplementary Figure 2

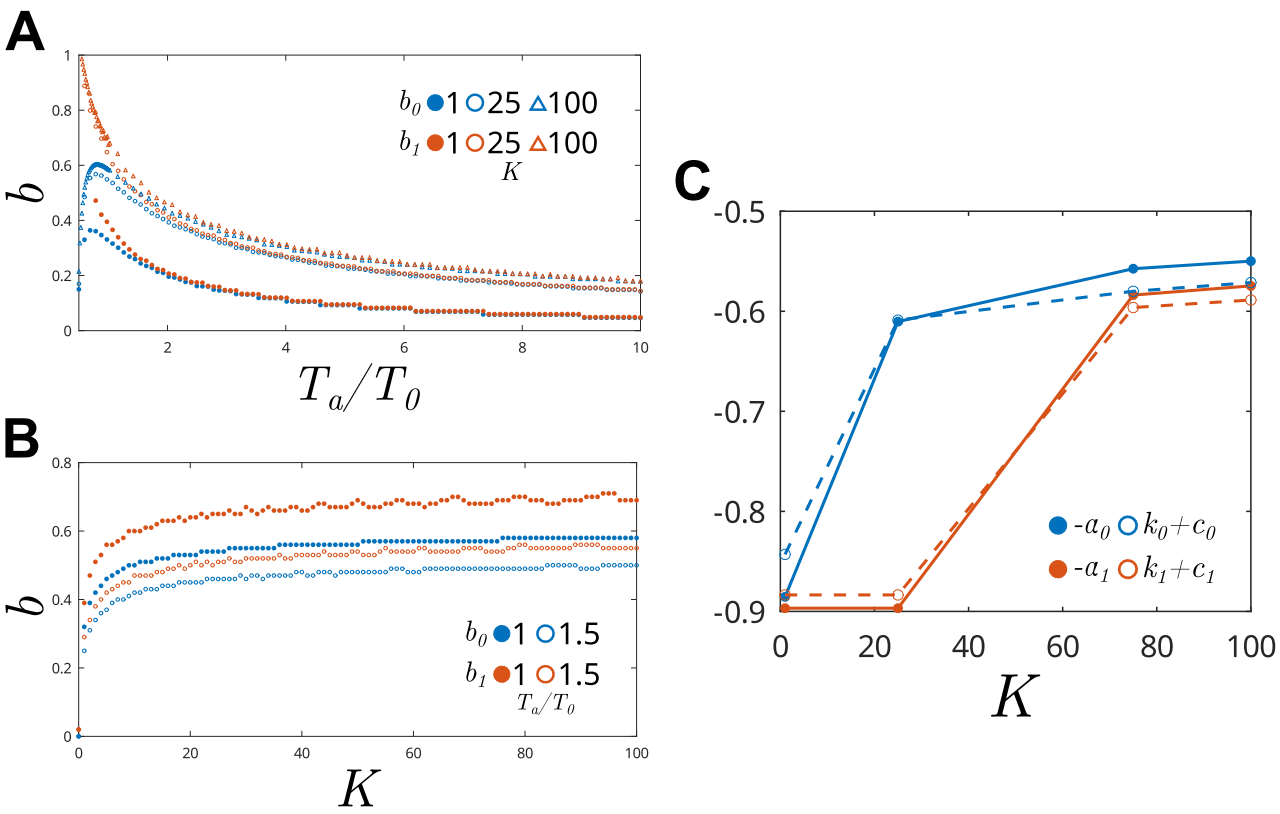


**Supplementary Figure 2: Dependence of curves $b_0$ and $b_1$ with parameter $K$.** (a) Plot of $b_0(T_a/T_0)$ and $b_1(T_a/T_0)$ for $K$ = *1, 25, 100*. Increasing $K$ makes $b_0$ and $b_1$ generally have larger values, although the difference becomes smaller for larger $K$. (b) Plot of $b0(K)$ and $b1(K)$ for $Ta/T0$ = *1, 1.5*. As shown in (a), at each $T_a/T_0$, both $b_0$ and $b_1$ grow monotonically with $K$, seemingly reaching an asymptote at high $K$. (c) Plot of parameters $k_0$, $k_1$ (open circles, broken lines), $-a_0$ and $-a_1$ (closed circles, lines) as functions of $K$, obtained by fitting $b_0(T_a/T_0)$ and $b_1(T_a/T_0)$ to a power-law equation $k(T_a/T_0)^{-a}$. Because values for $a_0$ and $k_0$ seemed to be parallel to each other, in order to better visualize them together we defined $c_0$ as the average difference between them, finding $c_0$ = *-1.2125*. Correspondingly for $a_1$ and $k_1$, we found $c_1$ = *-1.2756.*

**Supplementary Video 1:** Evolution in time of a simulated tissue in which extrusion occurs, as shown in Figure 7B. In this simulation the average cell width is $b = 0.5$ and $T_a/T_0 = 1.5$, which leads to extrusion. Although initially the tissue morphology seems to stabilize, several T1 transitions happen at $t = 11.8\,\tau_R$, causing the state of the tissue to change greatly. At $t = 20\,\tau_R$ the system has not yet reached a new equilibrium. That the stability threshold for tissues with $b = 0.5$ is between $T_a/T_0 = 1.5$ and $1.6$ is supported by the stability analysis performed on a simplified model.

**Supplementary Video 2:** Evolution in time of a simulated tissue in which extrusion does not occur, as shown in Figure 7C. In this simulation the average cell width is $b = 0.5$ and $T_a/T_0 = 1.6$. The time it takes for the energy to relax 90% into its final value is less than $t = \tau_R$, but in this example the tissue qualitatively can be seen to stabilize in around $6\,\tau_R$. That the stability threshold for tissues with $b = 0.5$ is between $T_a/T_0 = 1.5$ and $1.6$ is supported by the stability analysis performed on a simplified model.

## Appendix A

### A.1 Non-dimensional version of energy functional

For all simulations and for the following derivations, a non-dimensional version of the energy functional $E$ (eq. 1) was used. The formula can be obtained as $\epsilon = E/T_0 L_0$ , with $T_0$ being a characteristic surface tension equal to the surface tension of any cell-cell interface, and $L_0 = \sqrt{A_0} = \sqrt{K/P_0}$ a characteristic length, where $P_0$ is the pressure of the external medium. Using this, we obtain

$$\epsilon = \sum_{i,j} \frac{T_{ij}}{T_0}\frac{L_{ij}}{L_0} + \sum_i \frac{P_0 L_0}{T_0}\left(\frac{A_i}{A_0} - log\left(\frac{A_i}{A_0}\right)\right) + \frac{1}{2}\frac{K_n L_0}{T_0}\oint_{\partial C_i}\left(\frac{R_i(s) - r_i(s)}{L_0}\right)^2 H\left(\frac{R_i(s) - r_i(s)}{L_0}\right) ds \quad (A1)$$

where all variables are relative to $L_0$ and $A_0$ and three dimensionless parameter groups ($T_{ij}/T_0$, $P_0 L_0/T_0$ and $K_n L_0/T_0$) have been defined. We will use the dimensional and dimensionless names for these variables interchangeably throughout this appendix (i.e.: $E$ for $\epsilon$, $L_{ij}$ for $L_{ij}/L_0$, etc.).

### A.2 Force balance and shape of an interface at equilibrium (without nuclear overlap)

Two types of forces act on all vertices which don't interact with the nucleus: a tangential force coming from the surface tension term and a force derived from the pressure term in $E$ (eq. 1). Let $\vec{\alpha}$ be a 2-fold vertex on the boundary between cells $i$ and $j$ (any of which we might take as the external medium, substituting $A = 1/P_0$), with clockwise neighbour vertex $(x_-, y_-)$ and counter-clockwise neighbour $(x_+, y_+)$. Then the force acting on $\vec{\alpha}$ is given by:

$$\overrightarrow{F_\alpha} = -\frac{\partial E}{\partial \vec{\alpha}} = -\left\{\frac{\partial E}{\partial L_{ij}}\frac{\partial L_{ij}}{\partial \vec{\alpha}} + \frac{\partial E}{\partial A_i}\frac{\partial A_i}{\partial \vec{\alpha}} + \frac{\partial E}{\partial A_j}\frac{\partial A_j}{\partial \vec{\alpha}}\right\} \quad (A2)$$

Because $\partial L_{ij}/\partial\vec{\alpha} = -(\hat{t}_+ + \hat{t}_-)$ ( $\hat{t}_+$ and $\hat{t}_-$ being the tangent vectors pointing away from vertex $\vec{\alpha}$ ) and $\partial A_i/\partial\vec{\alpha} = \frac{1}{2}(y_+ - y_-, x_- - x_+) = -\partial A_j/\partial\vec{\alpha}$ (Fletcher *et al.*, 2013), we can rewrite equation (A2) as

$$\overrightarrow{F_\alpha} = \frac{T_{ij}}{T_0}(\hat{t}_+ + \hat{t}_-) + \frac{1}{2}\frac{P_0 L_0}{T_0}\left(\frac{1}{A_i} - \frac{1}{A_j}\right)(y_+ - y_-, x_- - x_+) \quad (A3)$$

We observe that $\hat{t}_{\alpha+} + \hat{t}_{\alpha-}$ always points in the average direction between the two edges and that $(y_+ - y_-, x_- - x_+)$ is perpendicular to the line between $(x_-, y_-)$ and $(x_+, y_+)$. In equilibrium $F_\alpha = 0$ and therefore the two terms in equation (A3) must be in the same direction (since $T_{ij} \neq 0$), meaning $\hat{t}_+ + \hat{t}_-$ is perpendicular to $(x_+ - x_-, y_+ - y_-)$. Since $\hat{t}_+ + \hat{t}_-$ bisects the angle between both edges, it follows that both edges must have the same length $l$, and since $(y_+ - y_-, x_- - x_+)$ has the same length as $(x_+ - x_-, y_+ - y_-)$, we may write

$$0 = T_{ij}\cos(\omega) - K\left|\frac{1}{A_i} - \frac{1}{A_j}\right| l \sin(\omega) \qquad (A4)$$

where $2\omega$ the inner angle between the two edges.

Since $T_{ij}$ and $\left|1/A_i - 1/A_j\right|$ depend only on the cells involved, the inner angle $2\omega$ is only a function of edge length, which is equal between any two adjacent 2-fold edges and therefore constant along an interface. This means that any interface between two cells (or between a cell and the external medium) with no overlapping nucleus approximates a circular arc at equilibrium. Additionally as expected, the edge curves towards the cell with the least pressure (largest area).

**A.3 Deduction of nuclear repulsion forces and relation to the model by Kim *et al* (2024)**

In vertices experiencing nuclear repulsion, $\overrightarrow{F_\alpha}$ includes terms of the form

$$\vec{F}_{i,\alpha} = -\frac{1}{2}\frac{K_n L_0}{T_0}\frac{\partial}{\partial\vec{\alpha}}\left\{\oint_{\partial C_i}(R_i(s) - r_i(s))^2 H(R_i(s) - r_i(s))\, ds\right\} \qquad (A5)$$

This derivative involves changes in both the path for the integral and the value of $r_i(s)$ along that path. The integral is only modified along subsequent straight paths $\gamma_-$ and $\gamma_+$ , which go from $\overrightarrow{x_-} = (x_-, y_-)$ to $\vec{\alpha} = (x_\alpha, y_\alpha)$ and from $\vec{\alpha}$ to $\overrightarrow{x_+} = (x_+, y_+)$, respectively. For example, the integral $I_-$along $\gamma_-$ can be written as

$$I_- = \int_a^b \left(R_i(s) - \left|t\vec{\alpha} + (1-t)\overrightarrow{x_-} - \overrightarrow{x_{N,i}}\right|\right)^2 |\vec{\alpha} - \overrightarrow{x_-}| dt \qquad (A6)$$

where $\overrightarrow{x_{N,i}} = (x_{N,i}, y_{N,i})$ is the nuclear center, $|\vec{v}|$ is the Euclidean norm, and where we have omitted the Heaviside function by only integrating in the interval where it is non-zero ($a$ and $b$ are both functions of $\vec{\alpha}$ with values in the interval $[0,1]$). This integral is of the form

$\int_{a(\vec{x})}^{b(\vec{x})} f(\vec{x},t)\,dt$ and therefore its derivative with respect to $\vec{\alpha}$ (i.e.: taken with respect to $\vec{x}$ and evaluated at $\vec{x} = \vec{\alpha}$) follows the Leibniz Integral Rule:

$$\frac{\partial}{\partial\vec{\alpha}}\left\{\int_{a(\vec{x})}^{b(\vec{x})} f(\vec{x},t)dt\right\} = f(\vec{\alpha},b)\frac{\partial b}{\partial\vec{\alpha}} - f(\vec{\alpha},a)\frac{\partial a}{\partial\vec{\alpha}} + \int_a^b \frac{\partial f}{\partial\vec{\alpha}}\,dt \qquad (A7)$$

with $a = a(\overrightarrow{\alpha})$, $b = b(\overrightarrow{\alpha})$. Since $a$ is the lower limit where the (smooth) integrand of equation A6 is positive, either $f(\vec{\alpha},a) = 0$ or $a$ is the beginning of the edge (i.e.: $a = 0$) in which case $(da/d\vec{x}) = 0$ at $\vec{\alpha}$. Applying a similar reasoning to $b$ simplifies equation (A7) to

$$\frac{\partial}{\partial\vec{\alpha}}\left\{\int_{a(\vec{x})}^{b(\vec{x})} f(\vec{x},t)dt\right\} = \int_a^b \frac{\partial f}{\partial\vec{\alpha}}dt \qquad (A8)$$

For simplicity, we assume circular/spherical nuclei –as in our simulations– and take $R_i(s) = R$. Rewriting $\overrightarrow{r_-}(t) = t\vec{\alpha} + (1-t)\overrightarrow{x_-} - \overrightarrow{x_{N,i}}$, differentiation of the integral along $\gamma_-$ (eq. A6) with respect to the position of vertex $\vec{\alpha}$ yields

$$\frac{\partial I_-}{\partial\vec{\alpha}} = \int_a^b (R - |\overrightarrow{r_-}(t)|)^2 \frac{\vec{\alpha} - \vec{x}_-}{|\vec{\alpha} - \vec{x}_-|} - 2t|\vec{\alpha} - \vec{x}_-|(R - |\overrightarrow{r_-}(t)|)\frac{\overrightarrow{r_-}(t)}{|\overrightarrow{r_-}(t)|}dt \qquad (A9)$$

Defining $\overrightarrow{r_+}(t) = (1-t)\vec{\alpha} + t\overrightarrow{x_+} - \overrightarrow{x_{N,i}}$ and redefining $a$ and $b$ appropriately, one may differentiate along $\gamma_+$, resulting in

$$\frac{\partial I_+}{\partial\vec{\alpha}} = \int_a^b -(R - |\overrightarrow{r_+}(t)|)^2 \frac{\overrightarrow{x_+} - \vec{\alpha}}{|\overrightarrow{x_+} - \vec{\alpha}|} - 2(1-t)|\overrightarrow{x_+} - \vec{\alpha}|(R - |\overrightarrow{r_+}(t)|)\frac{\overrightarrow{r_+}(t)}{|\overrightarrow{r_+}(t)|}dt \qquad (A10)$$

Finally, the nuclear repulsion force acting on vertex $\vec{\alpha}$ is proportional to the sum of both these integrals, that is

$$\vec{F}_{i,\alpha} = -\frac{1}{2}\frac{K_n L_0}{T_0}\left\{\frac{\partial I_+}{\partial\vec{\alpha}} + \frac{\partial I_-}{\partial\vec{\alpha}}\right\} \qquad (A11)$$

Our integral term in the energy functional $E$ may be seen as a potential for the repulsive interaction included by Kim *et al.* (2024) in their force-based model. Although the force derived from our model is not equal to that proposed by them, we may state a similarity in the formula for the total force arising from the repulsion of a single edge. This is equivalent to the sum of the derivatives of a single edge's path integral, differentiated with respect to the position of both of its endpoints. Using the integral along $\gamma_-$ as an example, we obtain a force $\overrightarrow{F_-}$ of the form

$$\overrightarrow{F_-} = -\frac{1}{2}\frac{K_n L_0}{T_0}\left\{\frac{\partial I_-}{\partial \vec{\alpha}} + \frac{\partial I_-}{\partial \overrightarrow{x_-}}\right\} = \frac{K_n L_0}{T_0}\int_a^b (R - |\overrightarrow{r_-}(t)|)|\vec{\alpha} - \vec{x}_-|\frac{\overrightarrow{r_-}(t)}{|\overrightarrow{r_-}(t)|}dt \qquad (A12)$$

Re-introducing the Heaviside function, parametrizing by arc-length and writing the edge length as $L_-$ we can write this as

$$\overrightarrow{F_-} = \frac{K_n L_0}{T_0}\int_0^{L_-}\left(\vec{R} - \overrightarrow{r_-}(x)\right)H(R - |\overrightarrow{r_-}(x)|)dx \qquad (A13)$$

which follows the form proposed by Kim *et al.* 2024 as $F_{\alpha\beta}$.

**A.4 Derivation of energy formula for wedge-shaped cells**

Without nuclei, the dimensionless energy functional (eq. A1) becomes

$$E = \sum_{i,j}\frac{T_{ij}}{T_0}L_{ij} + \frac{P_0 L_0}{T_0}\sum_i A_i - \log(A_i) \qquad (A14)$$

Therefore, all we need to determine its minima are formulas for the cell areas and interfacial lengths. Surface tension is $T_0$ at cell-cell and $T_a$ at apical/basal interfaces. The energy per cell is thus

$$E_{cell} = \frac{1}{2}L_l + \frac{T_a}{T_0}(L_a + L_b) + \frac{P_0 L_0}{T_0}\left(A - log(A)\right) \qquad (A15)$$

with $L_l$, $L_a$ and $L_b$ the lateral, apical and basal interface lengths, defined as in Figure A1a. The average cell width is $b = (b_a + b_b)/2$, equal to the sum of the apical (basal) widths of any two adjacent cells.

The apical/basal sides are circular arcs (Fig. A1b; see above) and we see that for a generic circular arc of base $b$ and angle $\theta$ with respect to baseline, the radius of curvature is given by $\rho = b/2sin(\theta)$. The arc length is then given by

$$L = 2\theta\rho = \frac{b\theta}{\sin(\theta)} \qquad (A16)$$

while the cap area is equal to

$$A = 2\int_0^{\frac{b}{2}}\sqrt{\rho^2 - x^2}dx - \eta b = \frac{b^2}{4}\left(\frac{\theta}{sin^2(\theta)} - \frac{1}{\tan(\theta)}\right) \qquad (A17)$$

where the integral corresponds to the shaded area in Fig. A1b, and we have substituted $\rho = b/2sin(\theta)$, $\rho^2 = \eta^2 + (b/2)^2$ and $\eta = b/2tan(\theta)$.

Finally, the interface lengths and total area are given by

$$L_l = \sqrt{h^2 + (b_b - b)^2}, L_a = (2b - b_b)\frac{\theta_a}{\sin(\theta_a)}, L_b = b_b\frac{\theta_b}{\sin(\theta_b)} \qquad (A18)$$

$$A = bh + \frac{{b_b}^2}{4}\left(\frac{\theta_b}{sin^2(\theta_b)} - \frac{1}{\tan(\theta_b)}\right) + \frac{(2b - b_b)^2}{4}\left(\frac{\theta_a}{sin^2(\theta_a)} - \frac{1}{\tan(\theta_a)}\right) \qquad (A19)$$

where we have substituted $b_a = 2b - b_b$ and $b_b - b_a = 2(b_b - b)$.

Although four variables (plus parameter $b$) appear in equations (A18) and (A19) (and consequently in $E_{cell}$), $\theta_a$ and $\theta_b$ are actually functions of $h$ and $b_b$. This can be proven by considering a 3-fold vertex in the tissue, defined by angles $\theta_a$, $\theta_b$ and $\phi$ (Fig. A1c). In the limit in which inter-vertex distance tends to 0, pressure-derived forces disappear (see eq. A3, A4), so the tensions must add up to 0 in equilibrium, that is

$$T_a\big(cos(\theta_b), sin(\theta_b)\big) + T_a\big(-cos(\theta_a), sin(\theta_a)\big) + T_0\big(sin(\phi), -cos(\phi)\big) = 0 \qquad (A20)$$

or equivalently

$$\cos(\phi) = \frac{T_a}{T_0}(\sin(\theta_b) + \sin(\theta_a))$$
$$sin(\phi) = \frac{T_a}{T_0}(\cos(\theta_a) - \cos(\theta_b)) \qquad (A21)$$

These equations can be solved by introducing variables $\alpha = (\theta_a + \theta_b)/2$ and $\beta = (\theta_a - \theta_b)/2$, so that

$$\cos(\phi) = 2\frac{T_a}{T_0}\sin(\alpha)\cos(\beta)$$
$$sin(\phi) = -2\frac{T_a}{T_0}sin(\alpha)sin(\beta) \qquad (A22)$$

Dividing the second equation of (A22) by the first, we obtain

$$\frac{b_b - b}{h} = tan(\phi) = -\frac{\frac{T_a}{T_0}}{\frac{T_a}{T_0}}\frac{2\sin(\alpha)\sin(\beta)}{2\sin(\alpha)\cos(\beta)} = -tan(\beta) \qquad (A23)$$

where we used the fact that $tan(\phi) = (b_b - b_a)/2h = (b_b - b)/h$ (Fig. A1a). Because $\theta_a, \theta_b \in (0, \pi/2)$ and $\theta_a < \theta_b$, there is only one value of $\beta \in (-\pi/2, 0)$ which satisfies equation A22. This means that $\phi = -\beta$, which in turn simplifies the first equation in A21 to

$$\frac{T_0}{2T_a} = sin(\alpha) \qquad (A24)$$

with angle $\alpha \in (0, \pi/2)$ being uniquely determined. From eq. A23 and A24 we obtain

$$\theta_{\frac{a}{b}} = arcsin\left(\frac{T_0}{2T_a}\right) \mp arctan\left(\frac{b_b - b}{h}\right) \qquad (A25)$$

which proves that $E_{cell}$ is a function of variables $h$ and $b_b$ only.

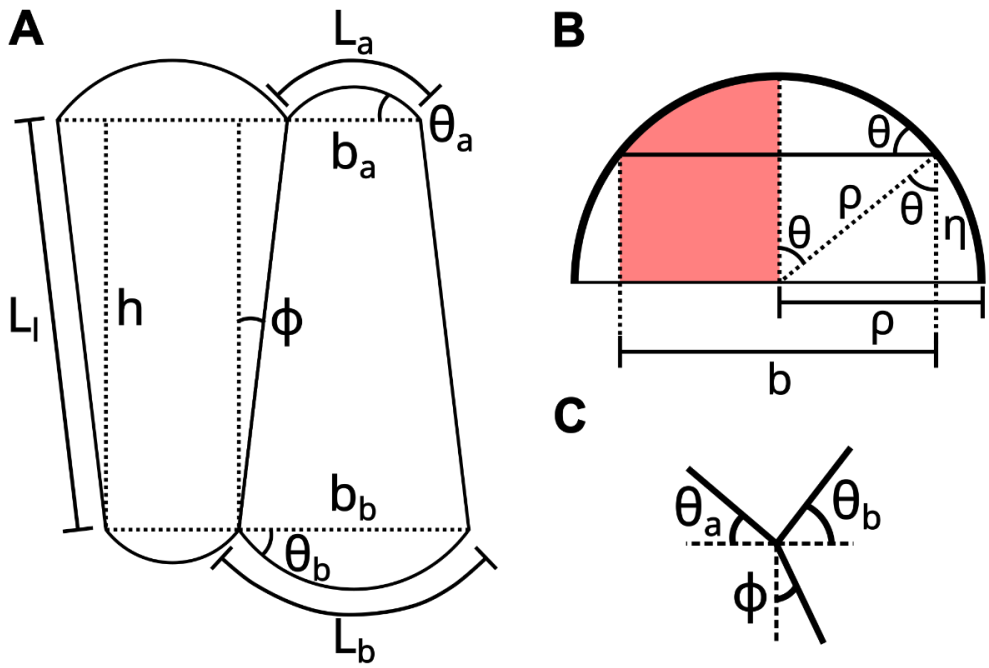


**Figure A1: Diagrams for the derivation of cell area and interfacial lengths in the simplified tissue composed of wedge-shaped cells. A**. Diagram of two neighbouring cells, indicating basal and apical widths ($b_b$ and $b_a$), contact angles ($\theta_b$ and $\theta_a$) and surface lengths ($L_b$ and $L_a$), as well as the lengths and angles for cell-cell contacts ($L_l$ and $\phi$). **B**. In the continuous limit, both the apical and basal caps are circular arcs with generic radius of curvature $\rho$, base $b$ and contact angle $\theta$. **C**. Diagram showing the relation between angles $\theta_a$, $\theta_b$ and $\phi$ at 3-fold vertices.

### A.5 Existence of a symmetrical single-layered equilibrium state

As seen in our analysis of a tissue composed of wedge-shaped cells, for fixed $L_0 = \sqrt{A_0} = \sqrt{K/P_0}$, a bifurcation in the energy minima happens as parameter $T_a/T_0$ increases, with extrusion ($b_b = 0$ or $b_b = 2b$) being favored for low $T_a/T_0$ and a symmetrical tissue

configuration in which $b_b = b_a = b$ becoming stable when $T_a/T_0$ is large. In fact, this equilibrium state exists for all values of $T_a/T_0 > 0.5$, indicating that this system undergoes a supercritical pitchfork bifurcation.

As this is a special case of a tissue composed of wedge-shaped cells, we search for solutions of $\nabla E_{cell} = 0$. Because of the tissue's symmetry, $E(b_b, h) = E(2b - b_b, h)$, which means $\partial E_{cell}/\partial b_b = 0$ when $b_b = b_a = b$. In that case, $\theta_{\alpha/\beta} = \theta = arcsin\left(\frac{T_0}{2T_a}\right)$, which necessitates $T_a/T_0 > 0.5$. Under these conditions, equations (A18-19) simplify to

$$L_l = h, \;\; L_a = b\frac{\theta}{\sin(\theta)} = L_b \qquad (A26)$$

$$A \; = bh + \frac{b^2}{2}\left(\frac{\theta}{sin^2(\theta)} - \frac{1}{\tan(\theta)}\right) \qquad (A27)$$

which depend only on variable $h$. Differentiating $E_{cell}$ (Eq. A15) with respect to $h$ gives us

$$dE_{cell} = \frac{1}{2} + \frac{P_o L_o}{T_0}\left\{b - \frac{b}{bh + \frac{b^2}{2}\left(\frac{\theta}{sin^2(\theta)} - \frac{1}{\tan(\theta)}\right)}\right\} = \frac{1}{2} + \frac{P_0 L_0 b}{T_0}\left\{1 - \frac{1}{A(h)}\right\} \qquad (A28)$$

which, when equal to 0, leads to

$$\left(\frac{T_0}{2P_0 L_0 b} + 1\right)^{-1} = A(h) = \; bh + \frac{b^2}{2}\left(\frac{\theta}{sin^2(\theta)} - \frac{1}{\tan(\theta)}\right) \qquad (A29)$$

from which $h$ may be obtained for any positive value of $b$, $P_0$ and $L_0$ as long as $T_a/T_0 > 0.5$.